Published in final edited form as:

NMR Biomed. 2010 August ; 23(7): 661–681. doi:10.1002/nbm.1520.

Theoretical models of the diffusion weighted MR signal†

Dmitriy A. Yablonskiy[a,b,*] and **Alexander L. Sukstanskii**[a]

[a]Department of Radiology, Washington University, St Louis, MO, USA

[b]Department of Physics, Washington University, St Louis, MO, USA

Abstract

Diffusion MRI plays a very important role in studying biological tissue structure and functioning both in health and disease. Proper interpretation of experimental data requires development of theoretical models that connect the diffusion MRI signal to salient features of tissue microstructure at the cellular level. In this review, we present some models (mostly, relevant to the brain) for describing diffusion attenuated MR signals. These range from the simplest approach, where the signal is described in terms of an apparent diffusion coefficient, to rather complicated models, where consideration is given to signals originating from extra- and intracellular spaces and where account is taken of the specific geometry and orientation distribution of cells. To better understand the characteristics of the diffusion attenuated MR signal arising from the complex structure of whole tissue, it is instructive to appreciate first the characteristics of the signal arising from simple single-cell-like structures. For this purpose, we also present here a theoretical analysis of models allowing exact analytical calculation of the MR signal, specifically, a single-compartment model with impermeable boundaries and a periodic structure of identical cells separated by permeable membranes. Such pure theoretical models give important insights into mechanisms contributing to the MR signal formation in the presence of diffusion. In this review we targeted both scientists just entering the MR field and more experienced MR researchers interested in applying diffusion methods to study biological tissues.

Keywords

diffusion; MRI; brain; phase contrast; membrane permeability; model selection; q-space analysis

INTRODUCTION

Diffusion MRI is a technique that is capable of providing *in vivo* images with a contrast uniquely sensitive to molecular displacement motion at cellular and sub-cellular length scales. Despite a rather long history and substantial progress in both clinical and research applications, the biophysical mechanisms underlying this contrast are not always understood. This is not surprising because biological tissues have very complicated

*Correspondence to: D. A. Yablonskiy, Mallinckrodt Institute of Radiology, Biomedical Magnetic Resonance Laboratory, Campus Box 8227, Washington University School of Medicine, 660 South Euclid Avenue, St Louis, MO 63110, USA., YablonskiyD@wustl.edu.

†This article is published in NMR in Biomedicine as a special issue on Progress in Diffusion-Weighted Imaging: Concepts, Techniques, and Applications to the Central Nervous System, edited by Jens H. Jensen and Joseph A. Helpern, Center for Biomedical Imaging, Department of Radiology, NYU School of Medicine, New York, NY, USA.

composition and geometrical architecture—factors that influence diffusion weighted MRI signal in multiple ways. For example, even a very small imaging MRI voxel positioned in the central nervous system (CNS) will always have a very complicated content due to the presence of myriads of cells with different sizes, intracellular milieu, membrane properties, etc. Consider that there are 10^7 neurons in 1 mm^3 of mouse cortex and each neuron has about 5 cm of axonal tree, 4 mm of dendrite tree and 8000 synapses; the average diameter of axons and dendrites is about 0.5 μm and 0.9 μm correspondingly; relatively large structures, like cell bodies with the size of 10 mm, occupy 12% of cortex volume while the rest is occupied by neuropil (34% by axons, 35% by dendrites, 14% by spines and 6% by extracellular space) (1). These statistical data represent gross approximations and are not always consistent among different published reports. Usually, extracellular space is assumed to occupy 15% to 20% of brain tissue (2,3), however, sometimes it is claimed to be negligible [2.5% in (4)].

The average diffusion coefficient for water in the CNS is about 1 μm^2/ms and the typical MR diffusion experiment employs a diffusion 20time Δ of –80 ms. Thus, the average water molecule probes a length scale on the order of 5–20 μm, making diffusion MR sensitive to a wide range of tissue microstructural parameters. The ultimate goal of MR diffusion theory is to quantitatively relate these microstructural and physiological parameters to the diffusion weighted MR signal. Due to the above mentioned highly complex tissue structure, these theories can never be perfect and can never ideally fit experimental data. However, as long as they reflect tissue properties of interest, they serve the purpose. The MR relevant range of length scales for restrictions and hindrances to water diffusion should be reflected in any model of MR diffusion data from biological systems. The critical issue is how best to do this. A few important effects should be taken into consideration:

- Molecules residing in the extracellular space will experience hindrances to their motion but, diffusion time permitted, could travel distances much longer than characteristic cellular sizes. For long diffusion times diffusion can be considered as quasi-Gaussian with a reduced ‘effective’ diffusion coefficient $Deff \approx Dfree/\lambda 2$, where λ is the tortuosity constant, $\lambda \sim 1.6$ under normal physiological conditions [see, for example, (3,5,6)].
- Molecules residing inside elongated cells, like axons and dendrites, will experience ‘guided’ diffusion that is practically Gaussian along the principal orientation axis of these cells and substantially restricted in the perpendicular directions.
- Molecules residing inside non-elongated cells will experience restricted diffusion in all directions.
- Depending on molecular species and cell types, cellular membranes might be considered either permeable or impermeable to molecular diffusion during time Δ of the MR experiment. For example, myelinated axonal membranes are practically impermeable to water and other metabolites. In other cells, like astrocytes, membranes are populated by aquaporins that greatly facilitate water transfer between intracellular and extra-cellular spaces (by orders of magnitude)

(7,8). The predominant CNS aquaporin family, aquaporin-4, has been found to be almost exclusively expressed in astrocytes (9).

A number of attempts have been made to incorporate these effects into theories of diffusion in biological tissues [see, for example, (10–21)]. While a comprehensive theory of diffusion in such a complicated environment remains under development, with contributions from many laboratories, in this review we will discuss how some of the above mentioned effects are reflected in the diffusion weighted MR signal.

STEJSKAL-TANNER EXPERIMENT

Most MR methods for measuring molecular displacement rely on a Stejskal-Tanner pulsed gradient (PG) experiment (22) with bipolar diffusion-sensitizing magnetic field gradient pulses. Here, the first gradient pulse, with a duration δ, encodes initial positions of nuclei through their MR signal phase and the second pulse, applied after time delay Δ (usually called diffusion time), decodes the final positions of these nuclei. The encoding and decoding gradient pulses shown in Figure 1 have either opposite polarity or are separated by a 180° refocusing RF pulse. From the point of view of the diffusion-attenuated MR signal, both sequences are identical (the difference becomes important when analyzing the influence of background gradients). For simplicity, all equations below are derived for the case of diffusion-sensitizing gradients of opposite polarity; however, all the final results are applicable for both cases.

In the case of sufficiently short gradient pulses, when molecular diffusion during time d can be ignored, each molecule accumulates phase only at two points of its trajectory: at its initial position $\mathbf{r}_0$ at time $t = 0, \varphi_0 = \gamma \mathbf{G} \mathbf{r}_0 \delta$, and at its final position $\mathbf{r}$ at time $t = T = \Delta$, $\varphi_T = \gamma \mathbf{G} \mathbf{r} \delta$

Here $\mathbf{G}$ is the field gradient and γ is the nuclear gyromagnetic ratio. The net MR signal after the bipolar gradient pulse can be written as:

$$S = S_0 \cdot \int\int_V d\mathbf{r} d\mathbf{r}_0 \rho(\mathbf{r}_0) P(\mathbf{r}, \mathbf{r}_0, \Delta) \exp[-i\gamma \mathbf{G}(\mathbf{r} - \mathbf{r}_0)\delta] \quad (1)$$

where $\rho(\mathbf{r}_0)$ is an initial spin density (usually, $\rho(\mathbf{r}_0)$ is homogeneous, $\rho(\mathbf{r}_0) = 1/V$); $P(\mathbf{r}, \mathbf{r}_0, \Delta)$ is a diffusion propagator describing the probability for a molecule to move from point $\mathbf{r}_0$ to point $\mathbf{r}$ during diffusion time Δ, S_0 is the MR signal amplitude without diffusion sensitizing gradients and integration is over all the initial and final positions of molecules in the system's volume V. The diffusion propagator $P(\mathbf{r}, \mathbf{r}_0, \Delta)$is a solution to the diffusion equation,

$$\frac{\partial P}{\partial t} = D \nabla^2 P \quad (2)$$

(D is the diffusion coefficient) with the initial condition $P(\mathbf{r}, \mathbf{r}_0, 0) = \delta(\mathbf{r} - \mathbf{r}_0)$, where $\delta(\mathbf{r} - \mathbf{r}_0)$ is the Dirac delta function, and with specific boundary conditions. Clearly, greater

molecule displacement during diffusion time Δ leads to a larger phase difference $(\varphi_T - \varphi_0)$ and stronger decay of the MR signal, Eq. [1]. Hence, the MR signal decay in the Stejskal-Tanner PG experiment is a measure of nuclear displacement. For an arbitrary pulse gradient waveform $\mathbf{G}(t)$ applied over a total time T, the phase accumulated by a molecule moving along a given trajectory $\mathbf{r} = \mathbf{r}(t)$ can be written as:

$$\varphi(T) = \gamma \int_0^T dt\, \mathbf{G}(t)\mathbf{r}(t)\,. \quad (3)$$

It is important to emphasize that the phase in Eq. [3] is determined not only by the initial and final positions of the molecule (as in the case of narrow pulses) but by all the points along the full displacement trajectory. To obtain the net diffusion attenuated MR signal, contributions of individual molecules should be averaged over all initial positions and possible trajectories (23):

$$S = S_0\langle \exp(-i\varphi(T))\rangle\,. \quad (4)$$

The expression in Eq [4] for the signal can also be presented in the form first proposed in (24):

$$S = S_0 \cdot \int_{-\infty}^{\infty} d\varphi P(\varphi)\exp(-i\varphi) \quad (5)$$

where $P(\varphi)$ is a distribution function for the phases in Eq.[4].

Another approach for calculating the MR signal is based on the Bloch-Torrey equation (25):

$$\begin{aligned} &\frac{\partial m(\mathbf{r},t)}{\partial t} = D\nabla^2 m(\mathbf{r},t) + i\gamma b_z(\mathbf{r},t)m(\mathbf{r},t), \\ &m(\mathbf{r},0) = \rho_0(\mathbf{r}) \end{aligned} \quad (6)$$

where $m(\mathbf{r}, t)$ is a circular component of transverse spatial magnetization distribution ($m = m_x + im_y$) at time t after the excitation RF pulse, and $b_z(\mathbf{r},t) = B_0 + \mathbf{G}(t)\cdot\mathbf{r}$. By solving this equation in the presence of Stejskal-Tanner gradients, one can then calculate an expression for the diffusion attenuated MR signal:

$$S = \int_V d\mathbf{r}\, m(\mathbf{r},T), \quad (7)$$

where integration is over the system volume V.

In the case of narrow pulses, the magnetization distribution $m(\mathbf{r}, \Delta)$ is given by (26):

$$m(\mathbf{r}, \Delta) = \exp(-i\gamma \mathbf{G}\mathbf{r}\delta) \cdot \int_V d\mathbf{r}_0 \rho(\mathbf{r}_0) P(\mathbf{r}, \mathbf{r}_0, \Delta) \exp(i\gamma \mathbf{G}\mathbf{r}_0\delta). \quad (8)$$

The above approaches for calculating the MR signal are tightly connected. They are similar to the Lagrangian and Eulerian descriptions of fluid dynamics. In the approach described by Eqs. [1]–[5], we are following the magnetization of diffusing molecules along their trajectories; in the Bloch-Torrey approach, Eqs. [6]–[8], we are looking at the magnetization distribution at a given spatial point **r** at a given diffusion time t.

UNRESTRICTED DIFFUSION

In a homogeneous unbounded media (e.g. water) thermal molecular motion is random, i.e. diffusion. In this case, the diffusion propagator $P(\mathbf{r}, \mathbf{r}_0, \Delta)$ has a well known Gaussian form:

$$P(\mathbf{r}, \mathbf{r}_0, \Delta) = \frac{1}{(4\pi D_0 \Delta)^{3/2}} \exp\left[-(\mathbf{r} - \mathbf{r}_0)^2 / 4D_0\Delta\right] \quad (9)$$

(this is why free diffusion is usually called ‘Gaussian diffusion’). Here D_0 is the free diffusion coefficient for water or other MR active species under consideration. For Gaussian diffusion, as in Eq. [9], MR signal decay given by Eq. [1] can be readily calculated. The result is a simple mono-exponential function (22):

$$S = S_0 \exp(-b\, D_0) \quad (10)$$

where b is the so-called b-value equal to $b = (\gamma G\delta)^2\Delta$ for the narrow pulse approximation. If signal attenuation during time is taken into account, the expression for b-value is (22):

$$b = (\gamma G\delta)^2 \left(\Delta - \frac{1}{3}\delta\right). \quad (11)$$

Equation [11] can also be obtained by solving the Bloch-Torrey equation, Eq. [6]. During the first gradient lobe in Figure 1, one finds that:

$$m(\mathbf{r}, t) = m(0) \cdot \exp(i\gamma\, \mathbf{G}\mathbf{r}\, t) \cdot \exp\left[-\frac{D_0}{3}(\gamma G)^2 t^3\right]. \quad (12)$$

Because during the first gradient lobe the magnetization has acquired a spatially varied phase, the magnitude of the local magnetization will continue to decay due to diffusion even

in the interval between lobes, $\delta < t < \Delta$, when $G = 0$. The solution to the Bloch-Torrey equation for this time interval is:

$$m(\mathbf{r}, t) = m(\mathbf{r}, t = \delta) \cdot \exp\left[-D_0(\gamma G\delta)^2(t - \delta)\right]. \quad (13)$$

Finally, after applying the second Stejskal-Tanner gradient lobe, we find:

$$\begin{aligned} & m(\mathbf{r}, t = \Delta + \delta) \quad (14) \\ & = m(\mathbf{r}, t = \Delta) \cdot \exp(-i\gamma \mathbf{G}\mathbf{r}\delta) \cdot \exp\left[-\frac{D_0}{3}(\gamma G)^2 t^3\right] = \\ & = m(0) \cdot \exp(-bD_0) \end{aligned}$$

which exactly coincides with Eq. [10] with b-value defined according to Eq. [11].

It is also important to emphasize that for free diffusion, Eq. [10] remains valid for an arbitrary diffusion-sensitizing gradient pulse waveform $\mathbf{G}(t)$ applied during a total time T, with b-value calculated according to equation (27):

$$b = \gamma^2 \int_0^T dt \left[\int_0^t dt' \mathbf{G}(t')\right]^2. \quad (15)$$

The results for different waveforms can be found in (28). Hence, by measuring MR signal intensity as a function of b-value and fitting Eq. [10] to the obtained MR signal, one can determine diffusion coefficient D_0.

GAUSSIAN PHASE APPROXIMATION

Another way to derive Eqs. [10]–[11] is based on Eq. [5]. Douglass and McCall (24) demonstrated for the case of free diffusion that the phase distribution function is of the Gaussian type

$$P(\varphi, T) = \frac{1}{\left(2\pi\left\langle\varphi^2(T)\right\rangle\right)^{1/2}} \exp\left[-\frac{\varphi^2}{2\left\langle\varphi^2(T)\right\rangle}\right]. \quad (16)$$

The MR signal corresponding to $P(\varphi, t)$ in Eq. [16] is equal to:

$$S = S_0 \cdot \exp\left[-\frac{1}{2}\left\langle\varphi^2(T)\right\rangle\right] \quad (17)$$

(without loss of generality, we consider . Averaging rather than the exponent in Eq. [4]] is a substantially less challenging problem because the expression for can be written in a closed form:

$$\langle \varphi^2(T) \rangle = \frac{2\gamma^2}{V} \int_0^T dt_1 \int_0^{t_1} dt_2 \int_V d\mathrm{r}_1 \int_V d\mathrm{r}_2 (\mathrm{G}(t_1)\mathrm{r}_1) \times (\mathrm{G}(t_2)\mathrm{r}_2) P(\mathrm{r}_1, \mathrm{r}_2, t_1 - t_2) \,. \quad (18)$$

In the case of unrestricted diffusion, when the propagator has a form of Eq. [9], the integrals in Eq. [18] can be readily calculated (24) leading to the same signal as in Eqs. [10]–[11].

If diffusion is restricted by some barriers or if the field gradients are non-uniform (as in the case of susceptibility-induced field inhomogeneities), the phase distribution function $P(\varphi, t)$, is, in general, not Gaussian. However, in some cases it can be well approximated by a Gaussian function in Eq. [16]—the so called Gaussian phase approximation (not to be confused with Gaussian diffusion). The quantity $< \varphi^2(T) >$ and, consequently, the signal in Eq. [17] can be readily calculated in systems for which the diffusion propagator $P(\mathbf{r}_1, \mathbf{r}_2, t)$ is available. Some important examples of these calculations can be found in (29).

In the Gaussian phase approximation $\left\langle \varphi^2(T) \right\rangle$ in Eq. [18] is proportional to the square of the diffusion gradient amplitude, hence can be written in the form $\left\langle \varphi^2(T) \right\rangle = G^2 \cdot f_\varphi$ where the function f_φ depends only on the timing of the diffusion sensitizing gradient waveform and the properties of the diffusing spins. Since b-value in Eq. [15] is also proportional to the square of the diffusion gradient amplitude, it can also be written in the form $b = G^2 \cdot f_b$ with f_b depending only on the timing of the diffusion sensitizing gradient waveform. Consequently, in the Gaussian phase approximation we can present the result for the diffusion attenuated MR signal in Eq. [17] as:

$$S = S_0 \cdot \exp(-b \cdot ADC), \quad ADC = \frac{1}{2}\frac{f_\varphi}{f_b}, \quad (19)$$

where ADC is the so called apparent diffusion coefficient (see further comments in the next section). As we demonstrated above, for free diffusion $ADC = D_0$ (i.e. the free diffusion coefficient). In general case, ADC depends on the ‘timing’ parameters of the gradient waveform and, of course, on the structure and properties of the environment in which spins diffuse. However, in the Gaussian phase approximation ADC does not depend on the strength of diffusion gradients (for fixed ‘timing’ parameters of the gradient waveform).

The quadratic dependence of ln S on the diffusion gradient G, ln $S \sim G^2$, is a 'hallmark' of the Gaussian phase approximation. The adequateness of the Gaussian phase approximation has been discussed by many authors (29–33). A detailed quantitative comparison of the Gaussian phase approximation with exact results for some models of restricted diffusion in the presence of a constant field gradient was given in (33) for a broad range of system parameters. First, this approximation is valid at short diffusion times, when phase accumulated by diffusing spins is small, $\varphi << 1$. Assuming that $\langle\varphi\rangle = 0$, one can get $\langle\exp(i\varphi)\rangle \approx 1 - \left\langle\varphi^2\right\rangle/2 \approx \exp(-\left\langle\varphi^2\right\rangle/2)$. Second, it can be valid at long diffusion times (this condition is necessary but not sufficient!), when all diffusing spins have encountered boundaries many times, their trajectories become statistically identical, and the central limit theorem can be applied. Obviously, this is not always true. For instance, in the case of narrow pulses, the diffusion attenuated MR signal from a single restricted compound demonstrates a quasi-periodic dependence on G [a so called 'diffusion diffraction' effect (30)]. An interesting regime with ln $S \sim G^{2/3}$was predicted in (34) and then confirmed in (35) in a model system.

ADC APPROACH

A simple and compelling temptation to describe the diffusion attenuated MR signal in biological tissues is to use an equation similar to Eq. [10] by introducing ADC:

$$S = S_0 \exp(-b \cdot ADC). \quad (20)$$

As we already discussed above, this approach is adequate in the Gaussian phase approximation with ADC defined by Eq. [19]. More generally, the ADC should be considered as a phenomenological parameter that incorporates integrative information on tissue microstructure. While it is quite insensitive to the details of this microstructure, it has played a very important role as a biomarker, especially in identifying pathology such as stroke (36). Usually, ADC is determined by measuring the diffusion attenuated MR signal at two b-values – zero and b, so that $ADC = \ln(S_0/S(b))/b$. This measurement however is not unambiguous because dependence of the diffusion attenuation MR signal on b-value in CNS is not mono-exponential. Numerous studies of the diffusion of water and/or other metabolites in brain tissue and other biological systems have documented this non-mono-exponential behavior of the MR signal S as a function of the b-value at fixed diffusion times (e.g. (12,37–48)). Originally this deviation of MR signal from mono-exponential behavior was treated as an evidence for a presence of two compartments and most authors reported that their data were fit well by a bi-exponential function with two different diffusion coefficients (large/fast and small/slow), ascribing the two exponential components to two physical compartments (extra- and intra-cellular) in a tissue. It is clear today that such a simple explanation is rarely valid. For example, Sehy *et al.* (49) have directly observed non-mono-exponential diffusion MR signal behavior even within the intracellular space of a single cell, the frog oocyte. In most *in vivo* experiments, each imaging or spectroscopic voxel contains numerous cells with different cell types, sizes, geometries, orientations, membrane permeabilities, and presumably different T2 and T1 relaxation time constants.

Practically any of the above-mentioned issues can lead to a deviation from mono-exponential behavior—a point clearly illustrated by Chin *et al*. (50). These authors carried out numerical simulations for a realistic geometrical structure of rat spinal cord and concluded that 'assignment of fractions obtained from biexponential fits of fast and slow diffusion attenuation to ECS and ICS volume ratios is not correct; rather, the observed multicomponent diffusion behavior is caused by motional restriction and limited inter-compartmental water exchange'. An insightful and entertaining discussion of this problem can be found in a recent paper by Mulkern *et al*. (51). Quite a few theoretical models have been proposed to explain this phenomenon. In this review we will discuss only several of them and show how different mechanisms could lead to non-mono-exponentiality of the diffusion attenuated MR signal, both in the simple situation of a single homogeneous compartment as well as in situations corresponding to the complexity of biological tissue.

KURTOSIS APPROACH

A model-independent way to quantify non-Gaussian water diffusion (when the MR signal's non-mono-exponentially depends on b-value) was proposed by Jensen *et al*. (52) (see also 53). It is based on a cumulant expansion of the signal $S(b)$, which is, in fact, a Taylor series of $\ln S(b)$:

$$\ln S(b) = -b\bar{D} + \frac{K}{6}(b\bar{D})^2 + \ldots \quad (21)$$

where K is a so called kurtosis. As shown in (52), in the narrow pulse approximation, the parameter K is related to the fourth moment of spin displacement. In the case of free (Gaussian) diffusion, when the spin displacement is described by the Gaussian distribution function, the kurtosis K in Eq. [21] (and all higher order terms in this expansion) is equal to 0. All tissue inhomogeneities (cell membranes, intracellular substructures, *etc*.) leading to non-Gaussian diffusion, contribute to the kurtosis K. In a simple one-dimensional system with impermeable boundaries, the kurtosis was calculated analytically in (54,55). Further details on Kurtosis approach and its applications in brain can be found in (56–58) and the review paper by Jensen *et al*. published in this issue of *NMR in Biomedicine*.

Even though such approach does not directly offer biophysical insight, it allows estimation of some empirical parameters related to tissue characteristics that might change with disease progression. Hence, such an approach may play an important role by providing an empirical biomarker of tissue status in health and disease (52).

STATISTICAL APPROACH

The ADC approach, Eq. [20], describes the MR signal in terms of an average apparent diffusion coefficient characterizing global properties of tissue in the imaging voxel. Given the tremendous complexity of tissue structure, the next logical step is to develop a strategy that would allow not only provide an evaluation of the mean diffusion coefficient but also the distribution of diffusion coefficients in the imaging voxel. In what follows, we introduce a statistical method/model (15) which reflects, in a well-defined manner, the consequences

of a distribution of length scales for restrictions and hindrances to diffusion. This general phenomenological model can describe a large number of experimental results related to the structure of the PG diffusion attenuated MR signal in biological systems.

Several rather general assumptions are made to describe the diffusion attenuated MR signal in terms of a statistical approach (15). It is assumed that the MR signal from a given voxel containing a variety of cells, and intercellular and extracellular spaces, can be described as a sum of signals from a large number of individual spin packets originating from different positions within the voxel. Because spin packets originate from different positions, travel through different displacement trajectories, and are confronted with different restrictions and hindrances to displacement, their individual contributions to the signal are described by Eq. [20] with different apparent diffusion coefficients:

$$ADC = ADC(\Omega;\ b), \quad (22)$$

where Ω represents a set of parameters that can be used to characterize (mark) spin packets. The ADC generally depends on the b-value, as was discussed in the previous section (Kurtosis approach). With this approach the total MR signal can be described in terms of a distribution function $F(\Omega)$ that gives the fraction of spin packets characterized by a given Ω:

$$S = S_0 \cdot \int d\Omega \cdot F(\Omega)\exp[-b \cdot ADC(\Omega;\ b)], \quad (23)$$

where the integration is over all values of parameters V. This expression is more general than was originally proposed in (15). In what follows, we will specify different distribution functions that depend on specific details of the biological system under consideration and on characteristics of the diffusion gradient waveform.

In case when the Gaussian phase approximation is valid, Eq. [23] can be reduced to:

$$S = S_0 \cdot \int_0^\infty dD\ P(D)\exp(-b\ D), \quad (24)$$

where $P(D)$ is simply a distribution function of ADCs. We should note, however, that $P(D)$ depends on the pulse gradient waveform structure (gradient direction, duration, shape and diffusion time). For the sake of simplicity, we keep these dependences in mind but omit them in the notations.

If the Gaussian phase approximation is not valid, the signal can still be formally represented in the form of Eq. [24], however, the function $P(D)$ loses its meaning as a distribution function of ADC. From mathematical point of view, the signal in Eq. [24] is a Laplace transform of the function $P(D)$, hence the inverse Laplace transform should reconstruct the function $P(D)$. However, the inverse Laplace transform requires knowledge of $S(b)$ in a

complex plane of b, and therefore is unavailable from experimental data. Employing a numerical approach to solve Eq. [24] from experimental data is a well known ill-posed problem [e.g. discussion in (59)].

For the limiting case of free diffusion, the distribution function is a d-function and the MR signal reduces to a mono-exponential, Eq. [10]. If a voxel were to contain several identifiable pools, the signal would be a discrete sum of weighted mono-exponentials. However, as noted earlier, biological tissue possesses an exceedingly complex structural micro-architecture and postulating a small number of identifiable pools to describe water displacement would seem counter intuitive. Indeed, it is far more likely that each of the large number of spin packets within a voxel experiences a net displacement somewhat different from all the other spin packets. Hence, we expect that the appropriate distribution function should be continuous rather than discrete. In the general case, its shape is rather complicated and we will consider different examples in corresponding sections below. In certain situations, however, quite general assumptions can simplify the problem. For example, if our system consists of numerous cells with relatively narrow distribution of cell sizes, we can expect that the distribution function $P(D)$ will be a peak-shaped with the peak width reflecting the width of cellular distributions (see example with HeLa cells below). If the distribution of cell sizes is not narrow but cellular membranes are permeable on the diffusion time scale and the diffusion time Δ is much longer than the characteristic time required for molecules to encounter a multitude of hindrances and restrictions to displacement, then diffusion is quasi-Gaussian and most spin packets can be expected to sample similar displacement trajectories and environments. This physical model also results in a peak-shaped distribution function, $P(D)$. The exact shape depends on the details of the structural micro-architecture within the voxel. However, under a realistic assumption that a large number of 'similar' cells reside in a voxel, the width of the distribution should be rather small and the 'tails' of the distribution should decay rather fast. Obviously, these assumptions can be satisfied by a Gaussian -type function:

$$P(D) = \begin{cases} A\exp\left[-(D - D_m)^2/2\sigma^2\right], & D > 0 \\ 0, D < 0 \end{cases} \quad (25)$$

where A is a normalization constant,

$$A^{-1} = \sigma\sqrt{\pi/2}\left[1 + \Phi\left(D_m/\sigma\sqrt{2}\right)\right], \quad (26)$$

D_m corresponds to the position of the distribution maximum (peak), σ is the width of the distribution, and Φ is the error function. The mean value of D (analog of ADC) in this model is equal to:

$$\bar{D} = \int_0^\infty dD \cdot P(D, D_m, \sigma) \cdot D = D_m + \sigma\sqrt{\frac{2}{\pi}} \cdot \frac{\exp(-D_m^2/2\sigma^2)}{[1 + \Phi(D_m/\sigma\sqrt{2})]}. \quad (27)$$

Substitution of Eqs. [25]–[26] in Eq. [24] gives an explicit expression for MR signal:

$$S = S_0 \frac{1 + \Phi(D_m/\sigma\sqrt{2} - b\sigma/\sqrt{2})}{1 + \Phi(D_m/\sigma\sqrt{2})} \exp(-b\,D_m + \frac{1}{2}b^2\sigma^2) \quad (28)$$

Note that both the exponential and pre-exponential factors are functions of b-value. In case of unrestricted diffusion, σ tends to zero and the distribution function $P(D)$ in Eq. [25] tends to a delta-function reducing the signal in Eq. [28] to Eq. [10].

For small b-values, Eq. [28] reduces to a mono-exponential function as in Eq. [10], however, as b grows, the decay rate becomes slower due to the positive term $b^2\sigma^2$=2. Nevertheless, the positive term $b^2\sigma^2$/2 never leads to signal growth because it is compensated for by a similar negative term in the pre-exponential error function. For large b-values, Eq. [28] decays as $1/b$:

$$S \to S_0 \cdot \left[\frac{\sqrt{2/\pi}\exp(-D_m^2/2\sigma^2)}{1 + \Phi(D_m/\sigma\sqrt{2})}\right] \cdot \frac{1}{b\sigma - D_m/\sigma} \quad (29)$$

It is also interesting to compare Eq. [28] with a cumulant expansion, Eq. [21]. Expanding ln $S(b)$Þ with $S(b)$ from Eq. [28] in

Taylor series, we get for the kurtosis K:

$$K = \frac{3}{\bar{D}^2} \cdot (\sigma^2 - \bar{D}^2 + \bar{D} \cdot D_m), \quad (30)$$

where $\bar{D}$ is given by Eq. [27]. It is important to emphasize that the statistical model, Eq. [28], can be used to describe diffusion attenuated MR signal for arbitrary b-values as it converges for large b-values (see Eq. [28]), while Eq. [21] can only be used for small b-values as it diverges for large b-values.

Applying this technique to a human brain, one can obtain images that describe the mean $\bar{D}$ values (or positions of distribution function maxima D_m) and the distribution width of these values for different anatomical regions. An example of such images is shown in Figure 2. Data were obtained on a whole body 1.5 T Siemens Magnetom Sonata. Axial 2D spin echo EPI images with b = 0.15, 0.3, .. ., 2.25 ms/μm^2 were taken for each direction of diffusion-

sensitizing gradients. Three orthogonal sets of diffusion sensitizing gradients (along the slice direction, along read-out and phase encoding directions) were applied.

Data from all brain tissues (except for CSF in ventricles) show substantial non-mono-exponential diffusion attenuation. The brightest regions in the D_m map correspond to CSF in ventricles and subarachnoid spaces. On the s map, CSF in ventricles is dark but remains bright at the ventricular edges and in subarachnoid spaces. The latter is most likely due to the partial volume effect (presence of tissue and CSF that have substantially different D_m in the same voxel) that leads to artificial broadening of the distribution function.

The average D_m across all ROIs for data shown in Figure 2 and Figure 3 is 0.90 ± 0.27 $\mu m^2/ms$ and the average s is 0.31 ± 0.07 $\mu m^2/ms$ or 36 ± 9% if calculated on a per voxel basis as a percentage of corresponding D_m. Similar results were found for other subjects.

These results demonstrate that for practically all human brain regions, the diffusion attenuated MR signal shows non-mono-exponential behavior that can be quantified in terms of a statistical model with a Gaussian-type distribution function in Eq. [25]. In this model, the mean diffusion coefficient $\bar{D}$ has a value close to ADC values determined previously by standard MR diffusion methods. It was also found that the distribution width σ was relatively constant across different brain tissues in both absolute units (about 0.3 $\mu m^2/ms$) and relative to ADC units (about 36%).

For very large b-values, the major contribution to the signal comes from slowly diffusing spin packets. If physical consideration of the object precludes the presence of spin packets with zero diffusivities, special care should be taken with regard to the behavior of the distribution function at small D because the Gaussian distribution Eq. [25] has a nonzero value at $D = 0$. Other distribution functions can be used to address this issue (see examples below). However, for a typical s of about 36% of ADC, which we found in a human brain, $P(D)$ reduces rapidly and for small D is proportional to $\exp(-0.5\, D_m^2/\sigma^2) \approx 0.02$. Also, due to this ‘narrowness’ of the distribution function, it remains symmetrical for most D, hence the difference between position of its maximum D_m and mean diffusion coefficient $\bar{D}$ is minimal.

We should note that applying the statistical approach with a Gaussian distribution function to brain tissue provides a phenomenological rather than structural description of diffusion in brain. It ignores specific details of the geometrical microstructure of cells, specifically - elongated geometry of axons and dendrites. These details will be addressed in the next sections of this review.

In the study by Zhao *et al.* (60), the statistical approach with the distribution function $P(D)$ given by Eq. [25] was used for analysis of experimental MR diffusion data obtained from cultured HeLa cells. Microbeads coated with HeLa cell monolayers were packed into a 6.0-mm-ID glass tube and perfused with pre-warmed and oxygenated media. The signal from intracellular water was measured in a broad range of diffusion times Δ--from 3 ms to 314 ms. Equation [28] provided an excellent fit to the signal from intracellular water, allowing estimation of the parameters D_m and σ. In experiments (60), the cells had a shape of hemi-

spheres of radius R. For this geometry, Zhao *et al.* found that for sufficiently long diffusion times $D_m = k \cdot \Delta^{-1}$; $k = 49R^2/320$. Thus, the slope of a plot of D_m vs. $1/\Delta$ yields an estimate of HeLa cell radius. The dependence of D_m on Δ^{-1} is shown in Figure 4. An average radius R found from these data is 10.1 μm and is in a good agreement with the average size of HeLa cells directly measured by optical microscopy.

Obviously, the truncated Gaussian distribution function, Eq. [25], is not a single choice for $P(D)$. For example, one can consider the distribution function based on the gamma distribution:

$$P(D) = \begin{cases} \frac{1}{D_m \Gamma(a)} \cdot \left(\frac{aD}{D_m}\right)^a \exp\left(-\frac{aD}{D_m}\right), & D > 0 \\ 0, & D < 0 \end{cases} \quad (31)$$

where $\Gamma(a)$ is the gamma-function. As well as $P(D)$ in Eq. [25], this distribution function is also characterized by two parameters: the position of the maximum, D_m, and the parameter $a > -1$ (note that for $a < 0$ the parameter $D_m < 0$ as well). The mean value of D and the signal S corresponding to the distribution function in Eq.[31] are as follows:

$$S = S_0 \cdot \left(\frac{a}{a + bD_m}\right)^{a+1}; \qquad \bar{D} = D_m \cdot \frac{a+1}{a} \quad (32)$$

The distribution functions in Eqs. [25] and [31] have infinite ‘tails’; that is not realistic because the diffusion coefficient D, obviously, cannot exceed the value of free diffusion coefficient D_0. This shortcoming is absent in the distribution function based on the classical beta-function:

$$P(D) = \begin{cases} \frac{1}{D_0} \cdot \frac{\Gamma(\alpha+\beta)}{\Gamma(\alpha)\Gamma(\beta)} \cdot \left(\frac{D}{D_0}\right)^{\alpha-1} \left(1 - \frac{D}{D_0}\right)^{\beta-1}, & 0 < D < D_0 \\ 0, & \text{otherwise} \end{cases}$$

(33)

The distribution function in Eq. [33] is characterized by two parameters: $\alpha > 0$ and $\beta > 0$. Generally speaking, the ‘free’ diffusion coefficient D_0 is usually also not known and, therefore, can be considered as a parameter as well. The mean value of D and the signal S corresponding to the distribution function in Eq. [33] are as follows:

$$S = S_0 \cdot F_{ch}(\alpha,\ \alpha+\beta;\ -bD_0); \qquad \bar{D} = D_0 \cdot \frac{\alpha}{\alpha+\beta} \quad (34)$$

where F_{ch} is the confluent hypergeometric function.

Summarizing, the statistical approach provides a framework for analysis of diffusion attenuated MR signal formation in complex biological systems. It relies on a statistical model that introduces a distribution function for the tissue *ADC*. At least two or three parameters are needed for each direction of the diffusion-sensitizing gradients to quantify diffusion in biological tissue with distributed parameters. This framework allows measurement of an intrinsic tissue specific *ADC* for a given diffusion time, independent of the strength of diffusion sensitizing gradients.

DIFFUSION ANISOTROPY--DTI MODEL

While accounting for complexity of CNS structure in a phenomenological manner, the statistical approach does not take into account the specific geometrical structure of cells. In particular, the presence of elongated cells, such as axons and dendrites, affects trajectories of diffusing molecules, making their diffusion along the main axes of these cells less obstructed than in a direction orthogonal to the main axes. Anisotropic diffusion creates the basis for diffusion tensor imaging (DTI) as proposed by Basser *et al*. (61). In this approach, diffusion is characterized by a diffusion tensor D_{ij} and Eq. [10] is transformed in:

$$S = S_0 \exp\left(-\sum_{i,j} b_{ij} D_{ij}\right) \quad (35)$$

where indices *i* and *j* are spatial coordinates x, y and z and:

$$b_{ij} = \gamma^2 \int_0^T dt \left[\int_0^t dt' G_i(t') \cdot \int_0^t dt' G_j(t')\right]. \quad (36)$$

Diffusion anisotropy is most important in white matter (WM) of CNS, but can also alter the diffusion attenuated MR signal in grey matter (GM) where diffusion is mostly isotropic on a macroscopic scale but is anisotropic on a microscopic scale (16,18) (see further discussion in the following sections of this article). Equation [35], while taking into consideration diffusion anisotropy, still assumes Gaussian diffusion, as in Eq. [9], only with different diffusion coefficients in different directions. DTI and its numerous derivatives are highly effective techniques to study CNS structure at the cellular level, both in health and disease. However, we will not discuss this subject here as numerous other reviews [see for example (62,63)], including several in this issue of *NMR in Biomedicine*, are devoted to this subject. In this review paper we will only discuss a few theoretical models that could provide a quantitative basis for studying diffusion anisotropy at the cellular level.

Tissue anisotropy and MR signal phase

Herein we should also mention another approach that provides information on the anisotropic structure of biological tissue from MRI experiments. As recently reported by Duyn *et al*. (64) and Marques *et al*. (65), the contrast in phase images of human and animal brains obtained with gradient recalled echo MRI at high fields holds great promise for the *in vivo* study of biological tissue structures with substantially improved resolution. The origins of this contrast were investigated by He and Yablonskiy (66) who demonstrated that this contrast depends on the tissue's 'magnetic architecture' at the sub-cellular and cellular levels. This architecture is mostly determined by the structural arrangements of proteins, lipids, non-heme tissue iron and deoxyhemoglobin, and their magnetic susceptibilities. This magnetic environment shifts the magnetic resonance frequencies of water molecules diffusing in the tissue. The theoretical framework developed in (66) is based upon the concept of a generalized Lorentzian approximation. This theory predicts the dependence of the signal phase on the orientation of WM fibers and thus holds promise as an additional tool for fiber tracking applications.

MICROSCOPIC DIFFUSION ANISOTROPY IN AXONS AND DENDRITES

As we already mentioned, an important characteristic of *in situ* neuronal structure is the high degree of anisotropy exhibited by neurons on the mm scale. Axons and dendrites are known to extend well beyond 10 mm, but are in most cases less than 2, or even 1 μm in diameter [see Table 1 in (67), for example]. While water molecules are present in all cells and interstitial spaces of the CNS, some of the metabolites, like *N*-acetyl-L-aspartate (NAA), are present mostly within the neuronal intracellular space making this molecule a useful endogenous probe for studying diffusion inside axons and dendrites. The extracellular NAA concentration is low (approximately 0.09 mM) (68), therefore the high concentration (>10 mM) of NAA known to exist in the brain (69–71) is localized to the neuronal intracellular space (71,72).

Evidence of the anisotropic NAA diffusion has been directly observed in the orientational dependence of NAA *ADC* measurements within the excised bovine optic nerve (39) and human corpus callosum (16). To incorporate this known property of neuronal structure into the analysis of diffusion data from NAA *in situ*, Kroenke *et al*. (16) introduced a relatively simple mathematical model similar to the one that had been previously derived in the study of gaseous ^{3}He diffusion in lung airspaces (73):

According to (16) the NAA MR signal from a large voxel within the brain represents a sum of signals from individual cellular structures. On the local scale, NAA displacements perpendicular to the approximately cylindrical (axonal or dendritic) structure are restricted because the diameter of these cellular structures (1–2 μm or less) is much less than the 'free' root-mean-squared displacement during a typical 50-ms diffusion time (~6 μm). Displacements parallel to the cylinder axis are, ideally, not restricted by cell membranes because axons and dendrites are known to be much longer than the ~10 μm. Using D_L and D_T to describe the apparent diffusion coefficients parallel and perpendicular to the cylinder axis, principal respectively, the diffusion-weighted MR signal obtained using a diffusionsensitizing gradient pair (Fig. 1) directed at some angle ϑ relative to the local cylinder axis is:

$$S = S_0 \exp(-b(D_L \cos^2\vartheta + D_T \sin^2\vartheta)) \quad (37)$$

Within a large voxel, or within grey matter, the NAA MR signal arises from many different neuronal structures that are oriented at different angles, ϑ, relative to the diffusion-sensitizing gradient pair. The MR signal is therefore:

$$S = S_0 \cdot \int_0^{\pi} d\vartheta \; P(\vartheta) \exp(-b(D_L \cos^2\vartheta + D_T \sin^2\vartheta)) \quad (38)$$

in which $P(\vartheta)$ is the distribution probability of cylinder axis orientations. We will introduce different distribution functions corresponding to different brain regions in the following section of this paper. Herein, we start from an assumption of an unbiased (macroscopically isotropic) distribution of neuronal structures where $P(\vartheta) = (\sin \vartheta)/2$. Then the expression for the MR signal becomes:

$$S = S_0 \exp(-bD_{\perp}) \left(\frac{\pi}{4b(D_L - D_T)}\right)^{1/2} \Phi\left((b(D_L - D_T))^{1/2}\right) \quad (39)$$

in which $\Phi(x)$ is the error function of x. This expression coincides with the one obtained for ^{3}He gas diffusion attenuated MR signal in lung (73,74). If the expected mean-squared displacement, $< \mathbf{r}^2 >$, perpendicular to neuronal extensions is equated with typical axon or dendrite diameters of less than 1 μm, the expected D of $< \mathbf{r}^2 > /4\Delta$ for diffusion time of 50 ms is extremely small (less than 0.01 μm^2/ms). Therefore, as a realistic first approximation, it can be assumed that $D_T \approx 0$. In this case, Eq. [39] simplifies to:

$$S = S_0 \cdot \left(\frac{\pi}{4bD_L}\right)^{1/2} \Phi\left((bD_L)^{1/2}\right) \quad (40)$$

an expression that has the same number of adjustable parameters (S_0 and D_L) as that for ADC model in Eq. [20]. Two important features are characteristic for the theoretical result in Eq. [40]. First we note that in contrast to Eq. [20] the signal dependence in Eq. [40] on b-value is substantially non-mono-exponential. Secondly, Eq. [40] predicts that, as long as diffusion length is smaller than the characteristic length of axons and dendrites, diffusion attenuated MR signal depends on diffusion time Δ only through the b-value.

Equation [38] has the general structure of a diffusion MR signal described by the statistical approach in Eq. [23], where parameters Ω correspond to the angles defining the orientation of cylindrical cells with respect to the direction of diffusion gradient. In this case, general Eq. [23] can also be reduced to a simplified form in Eq. [24]. Such a result can be obtained

by substituting $D = D_T + (D_L - D_T) \cdot cos^2\vartheta$ in Eq. [38], which reduces it to Eq. [24] with a 'powder-type' distribution function that reflects an unbiased distribution of cylinder directions:

$$P(D) = \begin{cases} \dfrac{1}{2[(D_L - D_T) \cdot (D - D_T)]^{1/2}}, & D_T < D < D_L \\ 0, \quad \text{otherwise} \end{cases} \tag{41}$$

Clearly, this function is very different from the Gaussian distribution function that reflects a symmetric peak-type distribution of diffusion coefficients.

To test these theoretical predictions, Kroenke *et al.* (16) obtained diffusion-weighted ^{1}H MR spectra, using multiple diffusion-sensitizing gradient settings, from five rats. Data were obtained froma large voxelcoveringa substantialpart of the brainofeachrat. To examine whether macroscopic anisotropy of NAA diffusion is present in the large volume selected for localized spectroscopy, diffusion was measured using Δ = 50 ms, and gradient pulses directed in three orthogonal directions. Only very slight systematic differences were seen in the comparison of data obtained with different diffusion-sensitization directions [Fig. 3a in (16)], indicating a small degree of macroscopic anisotropy.

The diffusion attenuated MR signal was also investigated over varying diffusion times (Δ from 50 to 100 ms), revealing practically no diffusion time dependence [Fig. 3b in (16)]—i.e. the signal depended only on *b*-value.

Figure 5 shows results of signal dependence on *b*-value for diffusion time Δ of 50 ms. To maximize the signal to noise ratio and to average any net diffusion anisotropy in the selected volume elements, the $S(b)$ curves corresponding to three orthogonal directions were summed together to generate the data plotted in Figure 5. The expected non-mono-exponential character of the NAA diffusion attenuation is clearly observed in Figure 5. Importantly, the theoretical, microscopically anisotropic, macroscopically isotropic model with $D_T = 0$ (hence only two adjustable parameters), given by Eq. [40], provides a close fit to the data. The D_L obtained from the fit displayed in Figure 5 is 0.36 ± 0.01 μm^2/ms. Attempts to determine the transverse diffusivity using the more general Eq. [39] and constraining D_T to be non-negative yielded the best fit at $D_T = 0$. This drawback however can be cured by a theory proposed recently by Sukstanskii and Yablonskiy (75) and discussed at the end of this section.

Figure 5 shows that, despite its simplicity, the diffusion model given by Eq. [40] provides an excellent fit to the experimentally measured $S(b)$ values, substantially better than the mono-exponential model in Eq. [20]. Quantitatively, Eq. [40] provides an almost 20-fold reduction in the χ^2 value compared to Eq. [20]. The obtained results are in agreement with other NAA *ADC* measurements. Indeed, as discussed in (76) and (73), for low *b*-values the exponential decay rate typically associated with the macroscopic *ADC* is the average of the three orthogonally-directed microscopic *ADC* values, $ADC = (D_L + 2D_T)/3$. Using D_L of 0.36

μm^2/ms and D_T of zero, an *in vivo* macroscopic ADC measurement using low b values is predicted to be 0.12 μm^2/ms. Literature reports of the NAA ADC obtained using smaller b-values than those employed by Kroenke *et al.* (16) closely match this predicted value (77).

As we already mentioned, the theory of NAA diffusion in brain tissue (Eq. [39]) is similar to the theory of ^{3}He gas diffusion in lung acinar airways (73,74). Recently, Sukstanskii and Yablonskiy (75) have demonstrated that a substantial improvement to the theory of ^{3}He gas diffusion in lung acinar airways can be achieved by including a non-Gaussian component that results from interaction of diffusing atoms with a sleeve of alveolar walls that create hindrances to atoms diffusing along lung acinar airways. Similar phenomenon, of course, might exist for molecules diffusing along axons and dendrites due to the presence of multiple intra-cellular structures as well as spines attached to cells' membranes (analog of alveoli in lung acinar airways). To include this effect, we need to substitute D_L in Eqs. [39] or [40] by:

$$D_L = D_{L0} \cdot (1 - \beta_L \cdot bD_{L0}) \quad (42)$$

where β_L is a parameter similar to kurtosis term in Eq. [21] and D_{L0} is a diffusivity of atoms/molecules diffusing along cells as determined in the limit of $bD_{L0} \rightarrow 0$. A similar term can also be included for transverse diffusion, however its contribution is negligible due to the overall smallness of the transverse diffusivity. Analyzing data shown in Figure 5, we find that D_{L0} = 0:39 μm^2/ms; D_T = 0:002 mm^2=ms and βL = 0:024. The contribution of the kurtosis term is small but noticeable--it changes the MRI-estimated longitudinal diffusion coefficient from D_{L0} = 0:39 μm^2/ms for small b-values to D_L = 0:32 μm^2/ms for b = 20 μs/mm^2. The longitudinal diffusion coefficient D_L = 0:36 μm/ms determined when the kurtosis term is not taken into account, is a weighted average over all b-values. Importantly, in this improved model, D_T is positive (as it should be) and very small, as expected.

In principle, further improvement in the model may be achieved by taking into consideration variations in fiber lengths and diameters and deviations from cylindrical symmetry in structures such as cell bodies. Meaningful parameter estimation from more elaborate signal models that account for these finer aspects of tissue structure will, however, require higher signal-to-noise experimental data.

Summarizing, based on the prior knowledge that NAA is confined to neuronal fibers and that a large number of fibers of varying orientations are present within a typical voxel used for NAA diffusion studies, a theoretical model that allows a quantitative description of the NAA diffusion MR signal has been proposed (16). The model fits experimental data strikingly well, and also provides a physical explanation of the previously observed deviation in the NAA diffusion signal from mono-exponential decay (38–40). Diffusion of NAA inside each individual fiber is strongly anisotropic, characterized by D_L of about 0.36 μm^2/ms and D_T of essentially zero. In contrast, the macroscopic diffusivity of NAA is practically isotropic due to averaging of fiber orientations. Given the kurtosis term is very small, it is reasoned that diffusion parallel to the fiber axes is only marginally affected by intra-cellular structures and spines.

WATER DIFFUSION IN BRAIN TISSUE

Previous section described theoretical model for NAA diffusion in brain tissue. It demonstrated that modeling diffusion attenuated MR signal as originated from multiple cylindrical compartments, provided an excellent fit to experimental data in a wide range of b-values (from 0 to $b\,D_L \approx 8$) using only two fitting parameters. To generalize this model for diffusion of water in brain tissue, we need to take into account that water is located both inside and outside the axons and dendrites with certain probability of exchange between 'in' and 'out' spaces. Here we describe such a theory developed by Jespersen *et al.* (18). The model is based on a simplified neural cytoarchitecture intended to capture the essential features important for water diffusion as measured by MR. Two components contribute to the signal in this model: (i) the dendrites and axons, which are modeled as long cylinders with two diffusion coefficients, parallel (D_L) and perpendicular (D_T) to the cylindrical axis (similar to the previous section of NAA diffusion), and (ii) an isotropic monoexponential diffusion component describing water diffusion within and across all other structures, i.e. in extracellular space and glia cells. A possibility for such separation rests on the observation that the water permeability of cell membranes differs by orders of magnitude, and most of this variability reflects the differential expression of aquaporin water channels (7,8). The predominant CNS aquaporin family, aquaporin-4, has been found to be almost exclusively expressed in astrocytes (9). The underlying assumption is that the water molecules have time to diffuse back and forth between glia cells and extracellular space, the diffusion coefficient thereby reflecting the average properties of both compartments. A promising aspect of this model is that it allows experimental access to several cytoarchitectural parameters noninvasively, one of the more interesting being the axon and dendrite density. This is a physiological variable that plays a central role in normal brain function and development and, as such, would be of great value for monitoring the progress of several diseases of the central nervous system.

Hence, in the approach proposed by Jespersen *et al.* (18), the diffusion signal is modeled as arising from two separate, non-exchanging components, one from compartments with cylindrical symmetry (dendrites and axons), s_c, and one from a compartment with spherical (isotropic) symmetry, s_i:

$$S = S_0 \cdot [(1-\nu)\, s_i + \nu s_c] \quad (43)$$

where ν is the volume fraction of water associated with cylinders (dendrites).

As a first approximation, the diffusion of water molecules not associated with the cylinders is modeled as isotropic Gaussian diffusion, i.e. a monoexponential diffusion signal $s_i \approx \exp(-bD_{eff})$. The effective diffusion constant D_{eff} reflects the tortuosity of the extra-cylindrical space, increased viscosity inside glia cells and hindrances imposed by their cell membranes.

Similar to the case of NAA, neuronal processes can be described as a collection of long cylinders contributing to the diffusion signal per Eq. [38]. It is assumed that on the timescale

of a typical diffusion experiment, the processes are nearly impermeable to water; this is necessary in order to enforce the strict compartmentalization required for the signal to be written as a sum of two contributions. Note that the mathematical treatment of the cylindrical diffusion process in Eq. [37] is only approximate, since interactions of the water molecules with the boundaries will add non-Gaussian corrections to the signal expression as discussed in the previous section; these effects are small and will be ignored here. In brain tissue, heterogeneous collections of cylinder orientations are encountered. The orientations of a collection of cylinders in a given voxel are described by $f(\theta,\ \varphi)d\Omega$, the fraction of dendrites or axons in the solid angle $d\Omega$ specified by spherical polar angles u and ‘ in the laboratory frame. In the white matter fiber tracts, the distribution of cylinders tends to peak along the direction of the fiber tract (78,79), whereas in grey matter, $f(\theta,\ \varphi)$ tends to be closer in appearance to a sphere. In general, $f(\theta,\ \varphi)$ can be expanded in spherical harmonics $Y_{lm}(\theta,\ \varphi)$:

$$f(\theta,\ \varphi) = \sum_{lm} f_{lm} Y_{lm}(\theta,\ \varphi)\,. \quad (44)$$

Experimental data demonstrate that $l = 2$ usually provides sufficient accuracy for describing data in grey matter with a total of 10 free parameters to be estimated in each voxel. In this case the explicit expression for the signal is:

$$S/S_0 = (1-\nu)e^{-b\,D_{\text{eff}}} + \nu\,\pi\,e^{-b\,D_T}\left\{f_{00}\left(\frac{\pi}{bD_A}\right)^{1/2}\Phi\left((bD_A)^{1/2}\right)Y_{00}(\theta,\ \varphi) + \right.$$
$$\left. + \left[\left(\frac{\pi}{4bD_A}\right)^{1/2}\Phi\left((bD_A)^{1/2}\right)\left(\frac{3}{2bD_A}-1\right) - \frac{3}{2bD_A}e^{-bD_A}\right]\sum_m f_{2m}Y_{2m}(\theta,\ \varphi)\right\}$$

where Φ is the error function and $D_A = D_L — D_T$. The first term for the cylindrical component in this expression coincides, of course, with Eq. [39] for NAA diffusion model.

Experimental data in (18) were obtained from an immersion- fixed brain from a two-day old baboon. One hundred and fifty three diffusion weighted images were acquired using a spin echo diffusion weighted pulse sequence with a nonselective 180° pulse. The diffusion parameters were δ/Δ =5ms/50ms, and 17 *b*-values ranging linearly from zero to 15 ms/μm^2. For each *b*-value, nine different orientations were selected from one hemi-sphere of an 18-point spherical 5-design (80), and this scheme was randomly rotated for each *b*-value.

Figure 6 displays results for main model parameters. The dendrite volume fraction shows relatively complex contrast across the brain: there is a thin superficial layer of relatively high volume fraction, followed by an extended subcortical region of somewhat lower values, and finally in the deeper brain regions the cylindrical volume fraction increases again. Average value for this parameter is 0.72. Sherwood *et al.* (81) measured the volume fraction of cell bodies (glia and neurons) in the primary motor cortex of anthropoid primates by Nissl staining, and found a value of approximately 15% in a 10-year old baboon. Assuming that the dendritic spines occupy approximately 14% of brain tissue (1) and neglecting

extracellular space [which is not always preserved in fixed tissue (3)], the volume fraction of cylindrical cells should be about 0.71, which is in a good agreement with our estimate of 0.72. This number also compares favorably with the total volume fraction of axons and dendrites in the mice brain [$v = 0.69$ (1)]).

The parallel cylindrical diffusion constant D_L averages to approximately 0.8 mm^2/ms, slightly less than half of the diffusion constant in the formalin (1.8 $\mu m^2/ms$). This difference can be explained by the viscosity of the intracellular fluid. Kroenke *et al.* (16) found, for NAA, that intracellular viscosity was the dominant determinant of D_L, and estimated this viscosity to be roughly twice that of a temperature matched dilute aqueous solution in agreement with the data of this study. Similar information was reported by Zhao *et al.* (82) for the intracellular diffusion constant in HeLa cells.

The effective diffusion constant D_{eff} varies between brain regions: in the internal capsule it has a value of about 0.2 $\mu m^2/ms$, and everywhere else it is about 0.3 to 0.5 $\mu m^2/ms$. The reduced value as compared with the average $D_L = 0.8 \mu m^2/ms$, reflects most likely tortuosity λ due to impermeable dendrites and resistance that water molecules encounter during motion between intracellular (glia) and extracellular spaces. If the tortuosity $\lambda = 1{:}6$ (5) of the extracellular space alone were responsible, a value of about $D_L/\lambda^2 \approx 0.3 \mu m^2/ms$ would be predicted in reasonable agreement with experimental data.

The transverse diffusivity D_T is much smaller than the other diffusion constants of the model. Its value is very small in white matter regions, about 0.03 $\mu m^2/ms$ in the internal capsule, which is similar to D_T of NAA reported in the previous section. However, it is higher in the grey matter where it averages about 0.1 $\mu m^2/ms$. This increase in grey matter D_T can be understood based on the assumption that D_T reflects non-vanishing permeability of the processes in the grey matter, where they are much less myelinated as compared to white matter.

The above described method deals with the situation when cylindrical cells form an arbitrary angular configuration in space. For simpler geometries when cylindrical cells form parallel configurations, similar methods were used by Assaf *et al.* (20) and Ong *et al.* (83) for evaluation of axonal diameter distributions. These authors found a rather good agreement between MR diffusion measurements and histological data.

Summarizing, a theoretical model of water diffusion in brain tissue developed by Jespersen *et al.* (18) contains two independent components, one with distribution of objects with cylindrical symmetry reflecting diffusion in dendrites and axons, and one with isotropic symmetry reflecting diffusion within and across all other structures. By describing the spatial distribution of cylindrical components within a voxel as a second order spherical harmonic expansion, the experimental data−-153 diffusion weighted images--are modeled quite well in most structures of a neonatal baboon brain. The obtained parameter values compare favorably to literature derived values and correlate well to DTI parameters. The possibility of measuring dendrite density shows a promising potential. Recently, Jespersen *et al.* (21) demonstrated that the model predictions of neurite density in rats are in good agreement with optical myelin staining intensity and stereological estimation of neurite

volume fraction using electron microscopy. Hence, the present framework constitutes an important step towards a better understanding of water diffusion in neural tissue.

A SINGLE-COMPARTMENT MODEL--EDGE ENHANCEMENT EFFECT

To better understand the characteristics of the diffusion attenuated MR signal arising from the complex structure of whole tissue, it behooves us to appreciate the characteristics of the signal arising from a single compartment or cell. First, we will describe a theory that deals with the spatial distribution of magnetization inside an idealized cell-like single compartment with impermeable membrane (84). Then we demonstrate how membrane permeability affects this magnetization distribution and, consequently, diffusion attenuated MR signal (26). In this review, major features of MR signal will be demonstrated using only one dimensional (1D) model of diffusion. Results for 2D and 3D cases are similar. In what follows we consider two extreme cases of Stejskal-Tanner pulse sequence in Figure 1--narrow pulse (NP) case when $\delta << \Delta$, and spin echo (SE) case when $\delta = \Delta$.

Consider 1D diffusion case when molecules diffuse between two infinite parallel planes positioned at $x = 0$ and $x = a$, and the gradient G applied along X axis. For the NP case, the expression for the signal is well known (22):

$$S = \frac{4\sin^2(qa/2)}{(qa)^2} + 4(qa)^2 \cdot \sum_{k=1}^{\infty} \frac{\exp\left(-(\pi k)^2 \cdot \Delta/t_D\right)\left[1-(-1)^k\cos(qa)\right]}{\left[(qa)^2-\pi^2k^2\right]^2}, \quad (46)$$

where $q = \gamma G\delta$ and $t_D = a^2/D_0$ is the characteristic diffusion time. The magnetization distribution can also be presented in an analytical form (26):

$$m(\mathrm{x},\Delta) = ie^{-iqx}\left\{\frac{1-e^{iqa}}{qa} + 2qa \cdot \sum_{k=1}^{\infty} \frac{\exp\left(-(\pi k)^2 \cdot \Delta/t_D\right)\cos(\pi k\,\mathrm{x}/a)\left[1-(-1)^k e^{iqa}\right]}{\left[(qa)^2-\pi^2k^2\right]^2}\right\} \quad (47)$$

[note here that we are using here the system size a rather than $2a$ in (84)].

For the SE case, our method is based on the random walk approach for describing spin's diffusion when spin's trajectories are divided into N small time intervals Δt, $t = N{\cdot}\Delta t$, and using the diffusion propagator $P(\mathbf{r}, \mathbf{r}_0, \Delta t)$ for describing spin's diffusion on each time interval (33). From the mathematical point of view, it is similar to the multiple pulse approximation proposed by Caprihan *et al.* (85) for calculating the net MR signal. Callaghan (86) reformulated this method in an elegant and simple-to-use form, which enables calculation of the signal for an arbitrary gradient waveform as a product of matrices. In (33), a similar approach has been used for calculating not only the net signal but the magnetization distribution as well.

The magnitude of the magnetization distribution $|m(x, \Delta)|$ is shown in Figure 7 for both NP and SE cases. The different curves in Figure 7 correspond to different values of the parameter

$$\alpha = \left(\frac{\Delta}{t_D}\right)^{1/2} = \frac{1}{a}(D_0\Delta)^{1/2} \quad (48)$$

As we see, for $\alpha = 0{:}05$ there is a substantial area in the center part of the compartment where the magnitude of magnetization $|m|$ is small and flat, whereas at the edges of the compartment it is significantly higher (edge enhancement effect). The physical origin of such an inhomogeneous magnetization distribution is rather simple: for sufficiently short diffusion times, when $\alpha << 1$ (the characteristic diffusion length $(D_0\Delta)^{1/2}$ is small compared to the system size a), diffusion of molecules located far from the boundaries can be considered as unrestricted and the decay of the transverse magnetization of these molecules can be described by an effective 'free' diffusion constant D_0. Diffusion of molecules located near the boundaries (at distance $\sim(D_0\Delta)^{1/2}$) is restricted due to encounters with the boundaries; here the decay of the transverse magnetization can be described by the *ADC* value D_1, $D_1 < D_0$. Calculations show that for $\alpha < 0{:}2$ the magnetizations in the center (m_0) and at the edges (m_1) are practically independent of a. Such a behavior allows for considering magnetization distribution in terms of two pools (or quasi-compartments): the magnetization in the central area (first pool), where diffusion can be considered as unrestricted, is $m_0 = \exp(-bD_0) \approx 0{:}368$ for $bD_0 = 1$. Whereas molecules located near the boundary (second pool) do not encounter the opposite boundary and therefore the value of D_1 is independent of the compartment size a. Therefore the value of m_1 in this regime is: $m_1 = \exp(-bD_1) \approx 0{:}7$ for the same b value ($bD_0 = 1$). With increase in Δ (the parameter α increases), the central region (first pool) narrows, whereas the region corresponding to the slow-diffusion component (second pool) broadens. As the number of spins encountering the boundaries increases with time as $\Delta^{1/2}$, it should be expected that the 'volume fraction' of the slow-diffusion component also scales as $\Delta^{1/2}$.

It is rather instructive to consider the MR signal in terms of the distribution function $P(D)$ introduced in Eq. [24]. It is easy to verify that for our case $P(D) = 1/|\partial D/\partial x|$, where $D(x, \Delta)$ is a 'local *ADC*' defined by Eq. [49]:

$$|m(x, \Delta)| = \exp(-bD(x, \Delta)) \quad (49)$$

The distribution function $P(D)$, for two different values of diffusion time: (a) $\alpha = 0{:}1$ ($\Delta = 0{:}01\ t_D$) and (b) $\alpha = 0{:}5$ ($\Delta = t_D$) is displayed in Figure 8 for the NP signal. In the short-time regime, $\alpha = 0{:}1$, the function $P(D)$ has two peaks located at $D = D_1$ and $D = D_2 \approx D_0$. These peaks correspond to slow and fast diffusing pools as described above and the relative heights and widths of the peaks reflect the pools' 'volume fractions'. Though peaks in the distribution $P(D)$ in the short-time regime are not exactly d-functions, all the spin can still be roughly divided into two pools and the net signal from the whole system can be well approximated in the form of the bi-exponential function:

$$S_{bi-\exp} = S_0 \cdot \left[\zeta \exp(-bD_1) + (1-\zeta)\exp(-bD_2)\right], \quad (50)$$

where S_0 is the signal in the absence of the diffusion sensitizing gradient, ζ is the 'volume fraction' of the slow-diffusing pool, and the parameters D_1 and D_2 can be associated with the *ADC*s of the slow- and fast-diffusion pools accordingly. For a α = 0:5, when the magnetization is practically flat, the function $P(D)$ has only one sharp maximum (Fig. 8b) and the signal can be well described as a single exponential (though kurtosis term is important for intermediate diffusion times).

To demonstrate an evolution of the parameters D_1, D_2, and ζ with diffusion time, the function in Eq. [50] was fitted to the net signal $S(b)$, generated by Eq. [46], in the interval $b \in [0, 2]$ for different diffusion times . The fit is extraordinarily good ($x^2 < 10^{-9}$) and stable with respect to initial values of the parameters (in contrast to (55), where instability of their fitting routine was reported). The results are shown in Figure 9. At $\alpha \to 0$, the volume fraction $\zeta \to 0$, *ADC* of the fast diffusing pool, D_2, as expected, tends to D_0, whereas *ADC* of slow diffusing poll, $D_1 \to 0.22D_0$ for the SE signal and $D_1 \to 0.30D_0$ for the NP signal. With diffusion time increases, D_1 and D_2 monotonically decrease and ζ increases.

For sufficiently short diffusion time Δ, the parameters ζ and D_2 depend on a linearly: $\zeta = k_1\alpha$,with $k_1 \approx 1.4$ for the SE signal and $k_1 \approx 1{:}2$ for the NP signal; $D_2 = D_0 \cdot (1 - k_2\alpha)$,where $k_2 = 0.84$ for the SE signal and $k_2 = 0{:}70$ for the NP signal. Using these results and expanding Eq. [50] for small b values, we can find the mean diffusion coefficient:

$$\overline{D} \simeq D_2 + \zeta(D_1 - D_2) = D_0 \cdot \left(1 - k_3(D_0\Delta)^{1/2} \cdot \frac{S}{V}\right), \quad (51)$$

$bD_0 \ll 1$, $\alpha \ll 1$, where S/V is a surface to volume ratio (= $2/a$ in our 1D case), $k_3 \approx 0{:}95$ for the SE signal and $k_3 \approx 0{:}76$ for the NP signal.

The result in Eq. [51] practically coincides with the one-dimensional analog of the short-time expansion of the ADC obtained by Mitra *et al.* for NP (87) and De Swiet and Sen for SE (34). (Note that in the one-dimensional case, the surface-to-volume ratio appearing in the general result of (34,87) is equal to $2/a$; the numerical coefficient in the corresponding equations of (34,87) should be tripled because in the system under consideration the direction of the field gradient with respect to the boundaries is fixed and angular averaging is absent). Hence, the comparison of our results with those obtained in (34,87) enables us to infer that the short-time behavior of the *ADC* derived in (34,87) is valid only under the additional condition $bD_0 << 1$. If this condition is not satisfied, more general bi-exponential expression for the diffusion signal in Eq. [50] can be employed.

For $\alpha > 0{:}2$, fitting of the signal to the bi-exponential function fails because the transition between center and edge regions becomes smooth and, therefore, the concept of two pools or 'quasi-compartments' becomes meaningless. For $\alpha > 1$, where all the spins encounter the boundaries, the local magnetization becomes uniform and increases with increasing a (motional narrowing regime).

Above we have discussed some properties of magnetization distribution and MR signal in the system when diffusion takes place between two infinite impermeable planes and with gradient applied perpendicular to the planes (1D model). Very similar results for the magnetization distribution and the net signal can be obtained in more complicated geometries, i.e. in a system when diffusion takes place within a cylinder with the gradient applied perpendicular to the cylinder principal axis (2D model) (84). Similar to the 1D model, at small diffusion time, when the parameter $\alpha = (\Delta/t_D)^{1/2} < < 1$, the net signal in the 2D system can also be approximated by the bi-exponential function in Eq. [50]. This result was directly verified experimentally by Milne and Conradi (88). In their study, the diffusion attenuated MR signal, measured from a tube filled with water, was fitted by the bi-exponential function in Eq. [50]. The parameters of the pulse sequence were chosen in such a way as to achieve the short diffusion time regime, where such a fit is possible. Figure 10 demonstrates an excellent fit of the bi-exponential function to the experimental signal.

It is important to note that the physical background of the bi-exponential behavior of the signal at short diffusion time (quasi-compartments) implies a certain upper limit for the diffusion time. For typical water diffusion coefficient in biological systems ~ 1 μm^2/ms and a cell size $a \sim 1$ μm, the characteristic diffusion time is $t_D \sim 1$ ms. Thus, the bi-exponential signal behavior due to the inhomogeneous magnetization distribution in the short diffusion time regime can be observed in such cells only at extremely short diffusion time, $\Delta < 0.1$ ms. Such experiments are almost beyond current technology [see however (89,90)]. Alternatively, for a currently achievable diffusion time $\Delta \sim 10$ ms, only much larger cells with $a \sim 25$ μm ($t_D \sim 600$ ms) or greater would reveal the short-time bi-exponential net signal behavior. In the experimental study by Takahashi *et al.* (91) of the Mauthner axon in the lamprey spinal cord (diameter ~ 40 μm), the authors analyzed ADC by means of high-resolution MRI with the voxel size ~ 19 μm and found the absence of diffusion coefficient anisotropy for diffusion time $\Delta = 11$ ms. This result is in agreement with above discussed theory because for $D_0 \approx 0.98$ μm^2/ms and $a = 40$ μm (91), $\alpha \approx 0.16$ and the radial magnetization distribution should have a clearly visible flat interval similar to that in Figure 7. If the voxel covers only the center part of the axon, the measured ADC is the 'local' ADC (in our terminology) and $ADC \approx D_1$ independent on direction of the diffusion sensitizing gradients.

Summarizing, at short diffusion times, the presence of diffusion-restrictive barriers (membranes) reduces effective diffusivity near the membranes and leads to an inhomogeneous spin magnetization distribution (edge enhancement effect). In this case, the MR signal reveals a quasi-two-compartment behavior and can be empirically modeled remarkably well by a bi-exponential function. These results may provide a framework for

interpretation of experimental MR data on water and metabolite diffusion in giant axons and large cells in CNS and other tissues.

THE ROLE OF MEMBRANES PERMEABILITY: 1D PERIODIC STRUCTURE

In the previous section, we discussed a single-compartment model in which spin diffusion is restricted by impermeable boundaries. Now we consider effects of membranes permeability using a 1D periodic structure of identical compartments of the size a separated by permeable membranes with permeability μ. Such a periodic system was analyzed numerically in (92); an analytical solution was obtained in (26).

In the periodic structure, the diffusion propagator is a piecewise function defined by diffusion Eq. [2] with boundary conditions on the interfaces between compartments, located at points $x = na, n = 0, \pm 1, \pm 2, ...$

$$\frac{\partial P_{n-1}}{\partial x} = \frac{\partial P_n}{\partial x}, \quad D_0 \frac{\partial P_n}{\partial x} = \mu(P_n - P_{n-1}) \qquad \text{at } x = na, \quad (52)$$

where $P_n = P_n(x, x_0, \Delta)$; denotes the propagator in the n^{th} compartment, $(n - 1)a \le x \le na$. The particular case $\mu = \infty$ corresponds to free diffusion; the case $\mu = 0$ corresponds to completely impermeable boundaries.

In the framework of the narrow pulse approximation, the signal S and the magnetization distribution $m(x; \Delta)$ are determined by Eqs. [1], [8] and are given by the following expressions (26):

$$m(x, \Delta) = 2i\tilde{q} \cdot \sum_j \frac{\exp(-k_j^2 \cdot \Delta/t_D)\exp(-iqx)\left[\cos\left(k_j(1 - x/a)\right) - \exp(i\tilde{q})\cos(k_j x/a)\right]}{\left(\tilde{q}^2 - k_j^2\right)\left[(2\tilde{\mu} + 1)\sin k_j + k_j \cos k_j\right]} \quad (53)$$

$$S = S_0 \cdot \frac{2\tilde{q}^2}{\tilde{\mu}} \cdot \sum_j \frac{\exp(-k_j^2 \cdot \Delta/t_D)k_j^2 \sin k_j}{\left(\tilde{q}^2 - k_j^2\right)^2\left[(2\tilde{\mu} + 1)\sin k_j + k_j \cos k_j\right]} \quad (54)$$

where $\tilde{q} = qa, \tilde{\mu} = \mu a/D_0$ (a reduced permeability), $t_D = a^2/D_0$. The sums in Eqs. [53]–[54] are over all non-negative roots k_j of the transcendental equation

$$2\tilde{\mu} \cdot (\cos k - \cos\tilde{q}) - k \sin k = 0. \quad (55)$$

In the case μ = 0, corresponding to the impermeable boundaries, Eqs. [53]–[54] reduce to Eqs. [46]–[47].

The spatial distribution of magnetization $m(x)$, while affected by permeability, is to some extent similar to that in a single-compartment model described in the previous section: at short diffusion times, $\Delta << t_D$, there are clearly distinguished maxima located close to the boundaries and substantial areas in the central parts of the compartments where the magnetization is uniform and diffusion is practically unrestricted, hence $|m| = \exp(-bD_0) \approx 0.368$ for $bD_0 = 1$. Thus, a concept of two pools is applicable, and the bi-exponential behavior of the signal is expected. At $\Delta/t_D \tilde{0}.1$ the maxima in $m(x)$ merge and at $\Delta/\delta \sim 0.1$, the magnetization is practically uniform everywhere and gradually increases with diffusion time.

Influence of permeability on the magnetization distribution is demonstrated in Figure 11 for short diffusion times when the inhomogeneity of magnetization is most pronounced. As expected, the magnetization of the fast-diffusing ‘pool’ in the central part at short diffusion times is independent of permeability, whereas the magnetization of the slow-diffusion ‘pool’ decreases due to the spin exchange across the boundaries

(corresponding diffusion coefficient increases, approaching D_0 as boundaries become permeable).

In the important limiting case $qa << 1$, the phase accumulated by molecules is small, and the signal in Eq. [1] is related to mean square displacement of molecules $\left\langle (\Delta x)^2 \right\rangle$,

$$S \approx S_0 \cdot \left(1 - \frac{q^2}{2}\left\langle (\Delta x)^2 \right\rangle\right) \approx S_0 \cdot \exp(-bADC), \quad (56)$$

where $b = q^2\Delta$ and

$$ADC = \frac{\left\langle (\Delta x)^2 \right\rangle}{2\Delta}$$

$$= D_0 \cdot \left[\frac{1}{12(\tilde{\mu}+1)^2} \cdot \frac{t_D}{\Delta} + \frac{\tilde{\mu}}{\tilde{\mu}+1} - 8 \cdot \frac{t_D}{\Delta} \cdot \sum_j \frac{\exp(-k_j^2 \cdot \Delta/t_D)\sin^2(k_j/2)}{k_j^3(k_j - \sin k_j)}\right],$$

where k_j are non-negative roots of transcendental equation

$$k\cot(k/2) + 2\tilde{\mu} = 0 \quad (58)$$

The dependences of the apparent diffusion coefficient ADC on permeability μ and diffusion time Δ are illustrated in Figure 12. It shows that ADC demonstrates a rather monotonic behavior as a function of diffusion time. For short diffusion times ADC reduces relatively fast as a square root of diffusion time and then approaches a plateau in a long time regime.

Both short and long time behavior of ADC depend on permeability. Naturally, in the case of free diffusion, $\mu \to \infty, ADC = D_0$. In the short time regime, $\Delta << t_D$, ADC takes the form:

$$ADC = D_0$$

$$\cdot \left\{ 1 - \frac{1}{4\tilde{\mu}^3} \left[1 - 4\tilde{\mu} \left(\frac{\tau}{\pi} \right)^{1/2} + 4\tilde{\mu}^2 \tau - \exp\left(4\tilde{\mu}^2 \tau \right) \left(1 - \Phi(2\tilde{\mu}\tau^{1/2}) \right) \right] \right\}$$

Where $\tau = \Delta / t_D$ and $\Phi(x)$ is the error function. In the case of $\Delta << D_0/4\mu^2$ Eq. [59] is further simplified to:

$$ADC = D_0 \cdot \left[1 - \frac{8}{3\pi^{1/2}} \frac{(D_0\Delta)^{1/2}}{a} + 2\frac{\mu\Delta}{a} + O(\Delta^{3/2}) \right]. \quad (60)$$

The first two terms in Eq. [60] are similar to those in a short diffusion time expansion of the ADC in the system with impermeable boundaries; in particular, the second term is a one-dimensional analog of a ‘surface-to-volume’ term found in (87). The term proportional to μ describes a contribution to ADC related to the finite permeability of the boundaries. At short times this contribution is small as compared to the surface-to-volume term as was previously noted in (10). Obviously, for high permeability, the approximation in Eq. [60] takes place only at very short diffusion times and is completely invalid in the limit of free diffusion, $\mu \to \infty$.

In the long-time regime, $\Delta > t_D$, the contribution from the sum in Eq. [57] is negligible and:

$$ADC = D_0 \cdot \frac{\mu a}{\mu a + D_0} + \frac{a^2}{12\Delta} \cdot \frac{D_0^2}{(\mu a + D_0)^2}. \quad (61)$$

In the case of impermeable boundaries, the ADC is inversely . proportional to diffusion time Δ: $ADC = a^2/12\Delta$, and tends to 0 at $\Delta \to \infty$. For any $\mu \neq 0$, ADC remains finite at any Δ. The first termin Eq. [61] was numerically found by Tanner (92), and noted by Crick (93) for the case of steady state diffusion between two distant points of a system such as ours.

Thus, under condition $qa << 1$, the signal depends on the parameter q and time Δ only in the combination $b = q^2\Delta$ and can be approximated by a mono-exponential in the b-value function in Eq. [56]. Obviously, this is not the case for arbitrary (qa) because the net signal, in general, depends on q and D in more complicated combinations (or doesn’t depend on D at all). For example, in the long-time regime, $\Delta >> t_D$, and small permeability, $\tilde{\mu} = \mu a / D_0 << 1$, the signal takes the form (26):

$$S = S_0 \cdot \mathrm{sinc}^2\left(\frac{qa}{2}\right) \cdot \exp\left(-4\sin^2(qa/2)\frac{\mu\,\Delta}{a}\right), \quad (62)$$

q-SPACE ANALYSIS OF 1D PERIODIC STRUCTURE

Equation [1] describing the signal in the NP approximation can be considered as a Fourier transformation of the average diffusion propagator

$$\bar{P}(X,\ \Delta) = \frac{1}{a}\int_0^a dx_0 P(x_0 + X, x_0, \Delta) \quad (63)$$

with respect to the spin displacement $X = (x - x_0)$. This propagator determines a probability for a molecule to diffuse a distance X during diffusion time Δ, averaged over the initial positions of the molecules. It can be calculated as an inverse Fourier transformation of the signal with respect to the parameter q (q-space imaging) (30):

$$\bar{P}(X,\ \Delta) = \frac{1}{2\pi}\int_{-\infty}^{\infty} dq \cdot S(q) \cdot \exp(i\ qX)\,. \quad (64)$$

In the case when the signal is mono-exponential in q^2 (as in Eq [56]), the average propagator $\bar{P}(X,\ \Delta)$ is Gaussian,

$$\bar{P}(X,\ \Delta) = \left(4\pi\bar{D}\Delta\right)^{-1/2}\exp\left(-X^2/4\bar{D}\Delta\right) \quad (65)$$

with $2\bar{D}\Delta = \left\langle X^2\right\rangle$ providing mean root square displacement of the particles. While in a general case $\bar{P}(X,\ \Delta)$ has a more complicated structure, it still can provide information on a system's geometry if properly analyzed (30,94). For example, for a 1D system with impermeable boundaries ($\mu = 0$), when the signal is given by Eq. [46], the average propagator is (94):

$$\bar{P} = u(X) \equiv (|X + a| + |X - a| - 2|X|)/2\,. \quad (66)$$

The function $u(X)$ has a well-known 'triangle' form (see Figure 13 below, dashed line) and is equal to 0 outside the interval $|X| \le a$. The 'full width at half maximum' (FWHM) of $u(X)$ in Eq. [66] is equal to a – the size of compartment. This very

important result led some investigators to believe that a similar relationship between FWHM of $\bar{P}(X,\ \Delta)$; and a characteristic compartment (i.e. cell) size should also exist for arbitrary

system of diffusing molecules. Below we demonstrate that using this assumption in systems with permeable membranes can lead to misleading conclusions.

For the periodic structure under consideration, in the long-time regime, $\Delta >> t_D$ and small permeability, $\mu << D_0/a$, when the signal is described by Eq. [46], the average propagator $\bar{P}(X, \Delta)$ can be readily calculated:

$$\bar{P}(X, \Delta) = \eta_0(\beta) \cdot u(X) + \sum_{n=1}^{\infty} \eta_n(\beta) \cdot [u(X - na) + u(X + na)]$$

$$\eta_n(\beta) = \exp(-\beta) \cdot I_n(\beta)$$

where $\beta = 2\mu\ \Delta/a, I_n$ are the modified Bessel functions, and $u(X)$ is given by Eq. [66]. In the case of impermeable boundaries, $\beta = 0$, only the term with $n = 0$ contributes to Eq. [67] and the function $\bar{P}(X, \Delta)$ coincides with Eq. [66]. In the case of finite permeability, $\bar{P}(X, \Delta)$ is a piecewise linear function of the displacement X. Examples of $\bar{P}(X, \Delta)$ are shown in Figure 13 for two values of the parameter β: $\beta = 0$ (line 1) and $\beta = 0{:}5$ (line 2).

It is clearly seen that the line 2 in Figure 13 creates the deceiving appearance of a multi compartment system with different compartment sizes, while it actually reflects the permeable nature of boundaries in a multi compartment system with a single compartment size. This effect should be taken into account for correct interpretation of experimental data derived by q-space imaging procedures in systems with permeable boundaries.

The structure of the average propagator in Eq. [67], which is a superposition of 'triangle' functions, allows a rather simple physical interpretation. Although for $\Delta > t_D$ the spins' spatial distribution is uniform and there exists no *spatially* distinct pools (in contrast to the short diffusion time regime), there exists an *implicit* differentiation of diffusing spins according to their 'diffusing history'. All the spins can be conditionally divided into populations discriminated by the average displacement traveled during diffusion time Δ. One group of spins travels a distance less than the compartment size a, most of spins of this group never leaving a compartment they have started from. The relative population--'weight'--of spins of this group is equal to $\eta_0(\beta) = \exp(-\beta) \cdot I_0(\beta)$. A second group comprises spins that sample two neighboring compartments, hence travel distances less than $2a$, its 'weight' is $\eta_1(\beta)$, and so on. In the case of impermeable boundaries, $\beta = 0$, only the first group of spins contributes to the sum in Eq. [67] and $\bar{P}(X, \Delta) = u(X)$. For barely permeable boundaries, $\beta << 1$, when only linear terms in b are taken into account, $\eta_1(\beta) \sim \beta \neq 0$, and the second group of spins becomes 'visible'; accounting for terms proportional to β^2 makes the third group 'visible' with $n = 2$, etc. Line 2 in Figure 13 corresponds to a rather small value of $\beta = 0{:}5$, and therefore the average propagator rapidly decreases with X (in Fig. 13 only the contributions of first 3 terms are 'visible'). As the parameter b increases, the central maximum $\bar{P}(0, \Delta)$ decreases whereas the width of $\bar{P}(X, \Delta)$ increases. In the limit $\beta >> 1$ (very long diffusion time), it can be approximated by the Gaussian envelope,

$$\bar{P}(X,\ \Delta) = \left(4\pi\bar{D}\Delta\right)^{-1/2}\exp\left(-X^2/4\bar{D}\Delta\right), \quad \bar{D} = \mu\, a, \quad (68)$$

though the piecewise linear structure of $\bar{P}(X,\ \Delta)$ holds for any β.

In essence, the presence of permeable boundaries has ‘discretized’ the spin population vis-a`-vis displacement distance. The physical background of this discretization is absolutely different from that in the system with impermeable boundaries in the short-time regime, when two ‘pools’ of spins can be distinguished by their locations with respect to the boundaries (Fig. 8). However, it also leads to a possibility to approximate the net signal in the long-time regime by the bi-exponential function in Eq. [49]. As shown in (26), such an approximation is possible if the permeability exceeds a certain threshold value μ_c depending on the diffusion time:

$$\mu_c = \frac{a}{120\Delta} \quad (69)$$

The condition $\mu > \mu_c$ implies a lower limit on the diffusion time Δ. For $\mu \sim 10^{-2}$ - 10^{-3} cm/s and cells with $a \sim 1$ μm, the condition $\mu > \mu_c$ is met for the diffusion time $\Delta > 1$ ms. The long diffusion time regime holds for such cells at $\Delta > t_D \sim 1$ ms. Consequently, the bi-exponential behavior of the signal, caused by finite membrane permeability, can be observed at typical experimental diffusion times (10 ms and longer).

Summarizing, finite permeability of cells membranes can substantially modify diffusion MR signal. In particular, the signal shape in the *q*-space might create the deceiving appearance of a multi-compartment system with different compartment sizes, while it actually reflects the permeable nature of boundaries in a multi-compartment system with a single compartment size. This effect should be taken into account for correct interpretation of experimental data derived by *q*-space imaging procedures in systems with permeable boundaries.

CONCLUDING REMARKS

In this review we have discussed several theoretical models for describing MR signals arising from brain tissue. As the brain is an extremely complex organ with great variability of structural units and parameters, it is not possible to propose a microscopically-based model which would be completely adequate. Thus, all the models discussed here and anywhere else are, in fact, phenomenological models with different levels of ‘phenomenologicity’.

The simplest pure phenomenological model is the *ADC* approach where the signal is described by a mono-exponential function, Eq. [20], with a single empirical parameter, *ADC*. The natural generalization of this model, accounting for a non-monoexponential dependence of the signal upon *b*-value, is the cumulant expansion in Eq. [21] proposed by Jensen *et al.* (52). Both these approaches have the ‘highest level of phenomenologicity’ because they do not make a direct attempt to relate their parameters to tissue microstructure

but rather to general properties of the MR signal. Yet, these parameters are reflective of tissue characteristics and might change with the disease progression. Hence, such approaches can play an important role by providing empirical biomarkers of tissue status in health and disease. Another type of phenomenological models is based on the statistical approach (15), where the tissue is characterized by a distribution of *ADC*s (or, in general, any other parameters) with different types of distribution functions as in Eqs. [23], Eqs. [24], [31]]–[34], etc. This approach is similar to that used in statistical physics to describe systems consisting of large numbers of particles, for example, gases and fluids.

On the opposite end of the spectrum of models are pure mathematical models allowing a detailed analysis of MR signal in idealized, very simple geometries (cylinders, spheres, *etc.*). Although such models cannot be directly applied to real systems, they give us some instructive clues as to how different biophysical parameters and processes affect MR signal formation. For example, a detailed analysis of a single-compartment model (84) revealed a mechanism that can result in bi-exponential behavior of the diffusion attenuated MR signal at short diffusion times. The analysis of a 1D periodic structure (26) demonstrated the important role of membrane permeability in the signal formation and, further, showed that the *q*-space analysis in systems with permeable membranes between compartments may lead to a substantially incorrect interpretation of experimental results if permeability is not incorporated into signal model. Hence, the suggestion, made by some investigators, that a *q*-space analysis could serve as a model-free tool for analyzing geometrical characteristics of different systems is not always correct and extreme caution should be exercised in applying this tool.

An important role is played by computer-based models of diffusion-attenuated MR signals. These models [see, e.g. (10–14, 50,95–97)] make it possible to calculate the signal in rather complicated systems comprised of multiple compartments. Such models can take into account different geometries of the compartments, their MR characteristics (e.g. T_1, T_2) and diffusion properties, as well as molecule exchange between compartments, *etc.*

A broad category of models lay between pure phenomenological and pure mathematical categories. Being partly phenomenological they, however, take into account some biophysical background of the specific tissue systems under consideration: specific geometries of cells, their spatial and oriental distributions, *etc*. By incorporating this preliminary information, such models attempt to grasp salient features of the system, relevant to a given experiment. If successful, important information on biological system structure can be obtained. Examples of such approaches considered in this review are a ‘cylindrical’ model of dendrites (16) that allowed an adequate description of the diffusion attenuated MR signal of the intra-axonal marker NAA, and its generalization to diffusion of water molecules in brain tissue (18).

Of course, such a ‘division’ of models in categories is conditional and is evolving with time. For instance, a very ‘popular’ 5–10 years ago bi-exponential model [e.g. (12,37–48)] was first suggested as having a biophysical basis reflecting the presence of intra- and extra-cellular spaces with different diffusivities. It is now apparent that such an interpretation is too simplistic and that a bi-exponential diffusion attenuated MR signal does not necessarily

proves the presence of two distinct tissue compartments. While in some cases a bi-exponential MR signal can obviously be related to tissue compartmentalization or geometrical structure, in most cases it simply reflects the fact that a bi-exponential function describes signal behavior better than does a mono-exponential function without a simple obvious relationship between the bi-exponential model's parameters and the physical parameters of the system under investigation. This is, of course, in agreement with conclusion of Chin *et al.* (50). An enlightening discussion of the bi-exponential model was provided by Mulkern *et al.* (51).

The category in which to place some recently proposed models is not clear yet. For example, a 'stretched exponent' model, $S = S_0 \exp\left[-(bD)^n\right]$, first proposed in (98) as a phenomenological model, may now be placed on a more biophysical foundation based on ideas of fractal geometry (99,100).

The natural question arises: which signal model should be used for a specific situation? This question has no general answer. The typical MR signal profile $S(b)$ is 'remarkably unremarkable' and usually can be fit by a variety of functions. Here we illustrate this by a simple example. The signal $S(b)$ was generated in the framework of the statistical model, Eq. [28], with parameters $D_m = 1\ \mu m^2/ms$ and $\sigma = 0{:}4\ \mu m^2/ms$, that are typical for brain tissue. Then the signal was fit by other models: (1) mono-exponential (Eq. [20]), (2) bi-exponential, (3) cumulant expansion truncated with three terms (kurtosis model, Eq. [21]), (4) cumulant expansion with four terms, (5) 'cylindrical' model (Eq. [39]), (6) 'stretched-exponent' model (98). The results are presented in Figure 14. As is obvious from Figure 14a, for $bD_m < 2$, the curves corresponding to all the models are almost indistinguishable. For $bD_m > 2$ only the curve corresponding to the mono-exponential function starts to deviate substantially from the signal. Only for $bD_m > 5$ do other models start to deviate from the signal generated by the statistical model. The results are more visible in the same graph if plotted on a log scale, Figure 14b. Although the best fit is provided by model #4 (cumulant expansion with four terms), in the interval realistic from an experimental point of view, when the signal has decayed to less than 10% of its initial amplitude, the fits are reasonably good for all the models. The signal in Figure 14 was generated in an ideal situation without noise. Model selection becomes even more challenging in experimental studies where noise is unavoidable.

So, how should a model be selected? Some have suggested this should be based upon studying the analytical properties of model functions in the complex plane of b-values (101). In our opinion, model selection should rather be based upon its ability to reflect the salient features of the biological structure under consideration, such as cell geometry, membrane permeability, *etc.* Of course, the model should be tested by fitting model parameters to the signal. In cases where prior information is unavailable, any phenomenological model that fits the data can be used, fitting parameters being considered as phenomenological biomarkers. Of course, some models fit data better than others. However, as demonstrated above, selection of the best model requires a very high SNR and a broad range of b-values.

And the last question: which domain to use for data analysis--b-domain that deals with the signal $S(b)$, or q-space domain when the signal $S(q)$ is analyzed? The answer is--it does not

matter since in both approaches the data are collected in exactly the same manner [see discussion of this issue in (51)]. Since the *q*-space analysis requires Fourier reconstruction of data, it is a subject to well known artifacts. From this perspective, the *b*-domain is preferable. Otherwise, it is simply a question of convenience and research goals. In both the cases we need a theoretical model if meaningful information of interest is to be extracted.

Acknowledgements

We would like to thank our colleagues Drs. Joseph Ackerman, Jeff Neil, Sune Jespersen, Chris Kroenke, Larry Bretthorst and Jim Quirk for numerous discussions of question related to diffusion in brain. Special thanks go to Joseph and Brenda Ackerman for careful reading and editing of our manuscript. This work was supported by NIH grants R01-NS055963, R01-HL70037, R01-EB002083 and U24-CA83060 as well as multiple grants from the NIH DRR Shared Instrumentation Grant (SIG) program.

REFERENCES

1. Braitemberg V, Schuz A. Cortex: Statistics and Geometry of Neuronal Connectivity Berlin: Springer; 1998.
2. Fishman RA. Cerebrospinal Fluid in Diseases of the Nervous System W.B. Saunders and Company; 1980.
3. Sykova E, Nicholson C. Diffusion in brain extracellular space. Physiol. Rev 2008; 88(4): 1277–1340. [PubMed: 18923183]
4. Rippe C, Rippe B, Erlanson-Albertsson C. Capillary diffusion capacity and tissue distribution of pancreatic procolipase in rat. Am. J. Physiol 1998; 275(5 Pt 1): G1179–1184. [PubMed: 9815049]
5. Diffusion Nicholson C. and related transport mechanisms in brain tissue. Rep. Progr. Physics 2001; 64(7): 815–884.
6. Mair RW, Hurlimann MD, Sen PN, Schwartz LM, Patz S, Walsworth RL. Tortuosity measurement and the effects of finite pulse widths on xenon gas diffusion NMR studies of porous media. Magn. Reson. Imaging 2001; 19(3–4): 345–351. [PubMed: 11445310]
7. Borgnia M, Nielsen S, Engel A, Agre P. Cellular and molecular biology of the aquaporin water channels. Annu. Rev. Biochem 1999; 68: 425–458. [PubMed: 10872456]
8. Solenov E, Watanabe H, Manley GT, Verkman AS. Sevenfold-reduced osmotic water permeability in primary astrocyte cultures from AQP-4-deficient mice, measured by a fluorescence quenching method. Am. J. Physiol. Cell. Physiol 2004; 286(2): C426–432. [PubMed: 14576087]
9. Amiry-Moghaddam M, Ottersen OP. The molecular basis of water transport in the brain. Nat. Rev. Neurosci 2003; 4(12): 991–1001. [PubMed: 14682361]
10. Latour LL, Svoboda K, Mitra PP, Sotak CH. Time-dependent diffusion of water in a biological model system. Proc. Natl. Acad. Sci. USA 1994; 91(4): 1229–1233. [PubMed: 8108392]
11. Szafer A, Zhong J, Gore JC. Theoretical model for water diffusion in tissues. Magn. Reson. Med 1995; 33(5): 697–712. [PubMed: 7596275]
12. Stanisz GJ, Szafer A, Wright GA, Henkelman RM. An analytical model of restricted diffusion in bovine optic nerve. Magn. Reson. Med 1997; 37(1): 103–111. [PubMed: 8978638]
13. Ford JC, Hackney DB, Alsop DC, Jara H, Joseph PM, Hand CM, Black P. MRI characterization of diffusion coefficients in a rat spinal cord injury model. Magn. Reson. Med 1994; 31(5): 488–494. [PubMed: 8015401]
14. Ford JC, Hackney DB, Lavi E, Phillips M, Patel U. Dependence of apparent diffusion coefficients on axonal spacing, membrane permeability, and diffusion time in spinal cord white matter. J Magn. Reson. Imaging 1998; 8(4): 775–782. [PubMed: 9702877]
15. Yablonskiy DA, Bretthorst GL, Ackerman JJ. Statistical model for diffusion attenuated MR signal. Magn. Reson. Med 2003; 50(4): 664–669. [PubMed: 14523949]
16. Kroenke CD, Ackerman JJ, Yablonskiy DA. On the nature of the NAA diffusion attenuated MR signal in the central nervous system. Magn. Reson. Med 2004; 52(5): 1052–1059. [PubMed: 15508157]

17. Sen PN, Basser PJ. A model for diffusion in white matter in the brain. Biophys. J 2005; 89(5): 2927–2938. [PubMed: 16100258]
18. Jespersen SN, Kroenke CD, Ostergaard L, Ackerman JJH, Yablonskiy DA. Modeling dendrite density from magnetic resonance diffusion measurements. NeuroImage 2007; 34(4): 1473–1486. [PubMed: 17188901]
19. Peled S New perspectives on the sources of white matter DTI signal. IEEE Trans. Med. Imaging 2007; 26(11): 1448–1455. [PubMed: 18041260]
20. Assaf Y, Blumenfeld-Katzir T, Yovel Y, Basser PJ. AxCaliber: a method for measuring axon diameter distribution from diffusion MRI. Magn. Reson. Med 2008; 59(6): 1347–1354. [PubMed: 18506799]
21. Jespersen SN, Bjarkam CR, Nyengaard JR, Chakravarty MM, Hansen B, Vosegaard T, Ostergaard L, Yablonskiy D, Nielsen NC, Vestergaard-Poulsen P. Neurite density from magnetic resonance diffusion measurements at ultrahigh field: comparison with light microscopy and electron microscopy. Neuroimage 2009; 49(1): 205–216. [PubMed: 19732836]
22. Stejskal EO, Tanner JE. Spin Diffusion Measurements: Spin Echoes in the Presence of a Time-Dependent Field Gradient. J. Chem. Phys 1965; 42(1): 288–292.
23. Abragam A Principles of Nuclear Magnetism New York: Oxford University Press; 1989.
24. Douglass DC, McCall DW. Diffusion in paraffin hydrocarbons. J. Phys. Chem 1958; 62: 1102–1107.
25. Torrey HC. Bloch Equations with Diffusion Terms. Phys Rev 1956; 104(3): 563–565.
26. Sukstanskii AL, Yablonskiy DA, Ackerman JJ. Effects of permeable boundaries on the diffusion-attenuated MR signal: insights from a one-dimensional model. J. Magn. Reson 2004; 170(1): 56–66. [PubMed: 15324758]
27. Karlicek RF, Jr, Lowe IJ. A Modified Pulsed Gradient Technique for Measuring Diffusion in the Presence of Large Background Gradients. J. Magn. Reson 1980; 37: 75–91.
28. Mattiello J, Basser PJ, LeBihan D. Analytical Expressions for the b Matrix in NMR Diffusion Imaging and Spectroscopy. J. Magn. Reson. Series A 1994; 108: 131–141.
29. Neuman CH. Spin echo of spin diffusion in a bounded medium. J. Chem. Phys 1973; 60(11): 4508–4511.
30. Callaghan PT. Principles of Nuclear Magnetic Resonance Microscopy New York: Claredon Press, Oxford; 1991.
31. Wang LZ, Caprihan A, Fukushima E. The narrow-Pulse Criterion for Pulsed-Gradient Spin-Echo Diffusion Measurements. J. Magn. Res. Series A 1995; 117: 209–219.
32. Stepisnik J Validity limits of Gaussian approximation in cumulant expansion for diffusion attenuation of spin echo. Physica B 1999; 270: 110–117.
33. Sukstanskii AL, Yablonskiy DA. Effects of restricted diffusion on MR signal formation. J. Magn. Reson 2002; 157(1): 92–105. [PubMed: 12202137]
34. de Swiet TM, Sen PN. Decay of nuclear magnetization by bounded diffusion in a constant field gradient. J. Chem. Phys 1994; 100(8): 5597–5604.
35. Hurlimann MD, Helmer KG, de Swiet TM, Sen PN, Sotak CH. Spin Echoes in a Constant Gradient and in the Presence of Simple Restriction. J. Magn. Reson 1995; A 113: 260–264.
36. Moseley ME, Cohen Y, Mintorovitch J, Chileuitt L, Shimizu H, Kucharc-zyk J, Wendland MF, Weinstein PR. Early detection of regional cerebral ischemia in cats: comparison of diffusion- and T2-weighted MRI and spectroscopy. Magn. Reson. Med 1990; 14(2): 330–346. [PubMed: 2345513]
37. Niendorf T, Dijkhuizen RM, Norris DG, van Lookeren Campagne M, Nicolay K. Biexponential diffusion attenuation in various states of brain tissue: implications for diffusion-weighted imaging. Magn. Reson. Med 1996; 36(6): 847–857. [PubMed: 8946350]
38. Assaf Y, Cohen Y. Non-mono-exponential attenuation of water and N-acetyl aspartate signals due to diffusion in brain tissue. J. Magn. Reson 1998; 131(1): 69–85. [PubMed: 9533908]
39. Assaf Y, Cohen Y. Structural information in neuronal tissue as revealed by q-space diffusion NMR spectroscopy of metabolites in bovine optic nerve. NMR Biomed 1999; 12(6): 335–344. [PubMed: 10516615]

40. Assaf Y, Cohen Y. In vivo and in vitro bi-exponential diffusion of N-acetyl aspartate (NAA) in rat brain: a potential structural probe? NMR Biomed 1998; 11(2): 67–74. [PubMed: 9608590]
41. Buckley DL, Bui JD, Phillips MI, Zelles T, Inglis BA, Plant HD, Blackband SJ. The effect of ouabain on water diffusion in the rat hippocampal slice measured by high resolution NMR imaging. Magn. Reson. Med 1999; 41(1): 137–142. [PubMed: 10025621]
42. Pfeuffer J, Provencher SW, Gruetter R. Water diffusion in rat brain in vivo as detected at very large b values is multicompartmental. Magma 1999; 8(2): 98–108. [PubMed: 10456372]
43. Mulkern RV, Zengingonul HP, Robertson RL, Bogner P, Zou KH, Gudbjartsson H, Guttmann CR, Holtzman D, Kyriakos W, Jolesz FA, Maier SE. Multi-component apparent diffusion coefficients in human brain: relationship to spin-lattice relaxation. Magn. Reson. Med 2000; 44(2): 292–300. [PubMed: 10918329]
44. Mulkern RV, Vajapeyam S, Robertson RL, Caruso PA, Rivkin MJ, Maier SE. Biexponential apparent diffusion coefficient parametrization in adult vs newborn brain. Magn. Reson. Imaging 2001; 19(5): 659–668. [PubMed: 11672624]
45. Clark CA, Le Bihan D. Water diffusion compartmentation and anisotropy at high b values in the human brain. Magn. Reson. Med 2000; 44(6): 852–859. [PubMed: 11108621]
46. Inglis BA, Bossart EL, Buckley DL, Wirth ED, 3rd, Mareci TH. Visualization of neural tissue water compartments using biexponential diffusion tensor MRI. Magn. Reson. Med 2001; 45(4): 580–587. [PubMed: 11283985]
47. Yoshiura T, Wu O, Zaheer A, Reese TG, Sorensen AG. Highly diffusion-sensitized MRI of brain: dissociation of gray and white matter. Magn. Reson. Med 2001; 45(5): 734–740. [PubMed: 11323798]
48. Ke Y, Cohen BM, Lowen S, Hirashima F, Nassar L, Renshaw PF. Biexponential transverse relaxation (T(2)) of the proton MRS creatine resonance in human brain. Magn. Reson. Med 2002; 47(2): 232–238. [PubMed: 11810665]
49. Sehy JV, Ackerman JJ, Neil JJ. Evidence that both fast and slow water ADC components arise from intracellular space. Magn. Reson. Med 2002; 48(5): 765–770. [PubMed: 12417990]
50. Chin CL, Wehrli FW, Hwang SN, Takahashi M, Hackney DB. Biexponential diffusion attenuation in the rat spinal cord: computer simulations based on anatomic images of axonal architecture. Magn. Reson. Med 2002; 47(3): 455–460. [PubMed: 11870831]
51. Mulkern RV, Haker SJ, Maier SE. On high b diffusion imaging in the human brain: ruminations and experimental insights. Magn. Reson. Imaging 2009.
52. Jensen JH, Helpern JA, Ramani A, Lu H, Kaczynski K. Diffusional kurtosis imaging: the quantification of non-gaussian water diffusion by means of magnetic resonance imaging. Magn. Reson. Med 2005; 53(6): 1432–1440. [PubMed: 15906300]
53. Lu H, Jensen JH, Ramani A, Helpern JA. Three-dimensional characterization of non-gaussian water diffusion in humans using diffusion kurtosis imaging. NMR Biomed 2006; 19(2): 236–247. [PubMed: 16521095]
54. Frohlich AF, Jespersen SN, Ostergaard L, Kiselev VG. The effect of impermeable boundaries of arbitrary geometry on the apparent diffusion coefficient. J. Magn. Reson 2008; 194(1): 128–135. [PubMed: 18619878]
55. Frohlich AF, Ostergaard L, Kiselev VG. Effect of impermeable boundaries on diffusion-attenuated MR signal. J. Magn. Reson 2006; 179(2): 223–233. [PubMed: 16406628]
56. Cheung MM, Hui ES, Chan KC, Helpern JA, Qi L, Wu EX. Does diffusion kurtosis imaging lead to better neural tissue characterization? A rodent brain maturation study. Neuroimage 2009; 45(2): 386–392. [PubMed: 19150655]
57. Falangola MF, Jensen JH, Babb JS, Hu C, Castellanos FX, Di Martino A, Ferris SH, Helpern JA. Age-related non-Gaussian diffusion patterns in the prefrontal brain. J Magn. Reson. Imaging 2008; 28(6): 1345–1350. [PubMed: 19025941]
58. Lazar M, Jensen JH, Xuan L, Helpern JA. Estimation of the orientation distribution function from diffusional kurtosis imaging. Magn. Reson. Med 2008; 60(4): 774–781. [PubMed: 18816827]
59. Epstein CL, Schotland J. The Bad Truth about Laplace's Transform. SIAM Rev 2008; 50(3): 504–520.

60. Zhao L, Sukstanskii AL, Kroenke CD, Song J, Piwnica-Worms D, Ackerman JJ, Neil JJ. Intracellular water specific MR of microbe-ad-adherent cells: HeLa cell intracellular water diffusion. Magn. Reson. Med 2008; 59(1): 79–84. [PubMed: 18050315]
61. Basser PJ, Mattiello J, LeBihan D. MR diffusion tensor spectroscopy and imaging. Biophys. J 1994; 66(1): 259–267. [PubMed: 8130344]
62. Le Bihan D, Van Zijl P. From the diffusion coefficient to the diffusion tensor. NMR Biomed 2002; 15(7–8): 431–434. [PubMed: 12489093]
63. Le Bihan D Looking into the functional architecture of the brain with diffusion MRI. Nat. Rev. Neurosci 2003; 4(6): 469–480. [PubMed: 12778119]
64. Duyn JH, van Gelderen P, Li TQ, de Zwart JA, Koretsky AP, Fukunaga M. High-field MRI of brain cortical substructure based on signal phase. Proc. Natl. Acad. Sci. USA 2007; 104(28): 11796–11801. [PubMed: 17586684]
65. Marques JP, Maddage R, Mlynarik V, Gruetter R. On the origin of the MR image phase contrast: an in vivo MR microscopy study of the rat brain at 14.1 T. Neuroimage 2009; 46(2): 345–352. [PubMed: 19254768]
66. He X, Yablonskiy DA. Biophysical mechanisms of phase contrast in gradient echo MRI. Proc. Natl. Acad. Sci. USA 2009; 106(32): 13558– 13563. [PubMed: 19628691]
67. Fiala GC, Harris CM. Dendrite structure. In Dendrites, Stuart G, Spruston N, Hausser M (eds). New York: Oxford University Press; 2001; 1–34.
68. Sager TN, Fink-Jensen A, Hansen AJ. Transient elevation of interstitial N-acetylaspartate in reversible global brain ischemia. J. Neurochem 1997; 68: 675–682. [PubMed: 9003055]
69. Burri R, Bigler P, Straehl P, Posse S, Colombo J-P, Herschkowitz N. Brain development: ^{1}H magnetic resonance spectroscopy of rat brain extracts compared with chromatiographic methods. Neurochem. Res 1990; 15: 1009–1016. [PubMed: 2077426]
70. Sager TN, Laursen H, Hansen AJ. Changes in N-acetyl-aspartate content during focal and global brain ischemia of the rat. J. Cereb. Blood Flow Metab 1995; 15: 639–646. [PubMed: 7790413]
71. Urenjak J, Williams SR, Gadian DG, M. N. Proton nuclear magnetic resonance spectroscopy unambiguously identifies different neural cell types. J. Neurosci 1993; 13: 981–989. [PubMed: 8441018]
72. Nadler JV, Cooper JR. N-acetyl-L-aspartic acid content of human neural tumours and bovine peripheral nervous tissues. J. Neurochem 1972; 19: 313–319. [PubMed: 4334499]
73. Yablonskiy DA, Sukstanskii AL, Leawoods JC, Gierada DS, Bretthorst GL, Lefrak SS, Cooper JD, Conradi MS. Quantitative in vivo assessment of lung microstructure at the alveolar level with hyperpolarized 3He diffusion MRI. Proc. Natl. Acad. Sci. USA 2002; 99(5): 3111–3116. [PubMed: 11867733]
74. Yablonskiy DA, Sukstanskii AL, Woods JC, Gierada DS, Quirk JD, Hogg JC, Cooper JD, Conradi MS. Quantification of lung microstructure with hyperpolarized 3He diffusion MRI. J. Appl. Physiol 2009; 107(4): 1258–1265. [PubMed: 19661452]
75. Sukstanskii AL, Yablonskiy DA. In vivo lung morphometry with hyperpolarized 3He diffusion MRI: theoretical background. J. Magn. Reson 2008; 190(2): 200–210. [PubMed: 18037313]
76. Callaghan PT, Jolley KW, Lelievre J. Diffusion of water in the endosperm tissue of wheat grains as studied by pulsed field gradient nuclear magnetic resonance. Biophys. J 1979; 28: 133–142. [PubMed: 262443]
77. Dreher W, Busch E, Leibfritz D. Changes in apparent diffusion coefficients of metabolites in rat brain after middle cerebral artery occlusion measured by proton magnetic resonance spectroscopy. Magn. Reson. Med 2001; 45: 383–389. [PubMed: 11241694]
78. Anderson AW. Measurement of fiber orientation distributions using high angular resolution diffusion imaging. Magn. Reson. Med 2005; 54(5): 1194–1206. [PubMed: 16161109]
79. Tournier JD, Calamante F, Gadian DG, Connelly A. Direct estimation of the fiber orientation density function from diffusion-weighted MRI data using spherical deconvolution. Neuroimage 2004; 23(3): 1176–1185. [PubMed: 15528117]
80. Hardin RH, Sloane NJA. McLaren's improved snub cube and other new spherical designs in three dimensions. Discrete Computational Geometry 1996; 15(4): 429–441.

81. Sherwood CC, Holloway RL, Erwin JM, Schleicher A, Zilles K, Hof PR. Cortical orofacial motor representation in Old World monkeys, great apes, and humans. I. Quantitative analysis of cytoarchitecture. Brain BehavEvol 2004; 63(2): 61–81.
82. Zhao L, Kroenke CD, Ackerman JJ, Neil JJ. The Intracellular Water Diffusion Coefficient of Cultured Microbead-Adherent HeLa Cells is >= 1 æm^2/ms. Proceedings of 14th Scientific Meeting and Exhibition, ISMRM 2006.
83. Ong HH, Wright AC, Wehrli SL, Souza A, Schwartz ED, Hwang SN, Wehrli FW. Indirect measurement of regional axon diameter in excised mouse spinal cord with q-space imaging: simulation and experimental studies. Neuroimage 2008; 40(4): 1619–1632. [PubMed: 18342541]
84. Sukstanskii AL, Ackerman JJ, Yablonskiy DA. Effects of barrier-induced nuclear spin magnetization inhomogeneities on diffusion-attenuated MR signal. Magn. Reson. Med 2003; 50(4): 735–742. [PubMed: 14523959]
85. Caprihan A, Wang LZ, Fukushima E. A Multiple-Narrow-pulse Approximation for Restricted Diffusion in a Time-Varying Field Gradient. J. Magn. Reson. Series A 1995; 118: 94–102.
86. Callaghan PT. A simple matrix formalism for spin echo analysis of restricted diffusion under generalized gradient waveforms. J. Magn. Reson 1997; 129(1): 74–84. [PubMed: 9405218]
87. Mitra PP, Sen PN, Schwartz LM. Short-time behavior of the diffusion coefficient as a geometrical probe of porous media. Phys. Rev. B 1993; 47(14): 8565–8574.
88. Milne ML, Conradi MS. Multi-exponential signal decay from diffusion in a single compartment. J. Magn. Reson 2009; 197(1): 87–90. [PubMed: 19121965]
89. Parsons EC, Jr, Does MD, Gore JC. Temporal diffusion spectroscopy: theory and implementation in restricted systems using oscillating gradients. Magn. Reson. Med 2006; 55(1): 75–84. [PubMed: 16342147]
90. Xu J, Does MD, Gore JC. Quantitative characterization of tissue microstructure with temporal diffusion spectroscopy. J. Magn. Reson 2009.
91. Takahashi M, Hackney DB, Zhang G, Wehrli SL, Wright AC, O'Brien WT, Uematsu H, Wehrli FW, Selzer ME. Magnetic resonance micro-imaging of intraaxonal water diffusion in live excised lamprey spinal cord. Proc. Natl. Acad. Sci. USA 2002; 99(25): 16192– 16196. [PubMed: 12451179]
92. Tanner JE. Transient diffusion in a system partitioned by permeable barriers. Application to NMR measurements with a pulsed field gradient. J. Chem. Phys 1978; 69(4): 1748–1754.
93. Crick F Diffusion in Embriogenesis. Nature 1970; 225: 420–422. [PubMed: 5411117]
94. Cory DG, Garroway AN. Measurement of translational displacement probabilities by NMR: an indicator of compartmentation. Magn. Reson. Med 1990; 14(3): 435–444. [PubMed: 2355827]
95. Novikov DS, van Dusschoten D, van As H. Modeling of Self-Diffusion and Relaxation Time NMR in Multi-Compartment Systems. J. Magn. Reson 1998; 135: 522–528. [PubMed: 9878479]
96. van der Weerd L, Melnikov SM, Vergeldt FJ, Novikov EG, Van As H. Modelling of self-diffusion and relaxation time NMR in multicompartment systems with cylindrical geometry. J. Magn. Reson 2002; 156(2): 213–221. [PubMed: 12165256]
97. Hwang SN, Chin CL, Wehrli FW, Hackney DB. An image-based Finite Difference Model for Simulating Restricted Diffusion. Magn. Reson. Med 2003.
98. Bennett KM, Schmainda KM, Bennett RT, Rowe DB, Lu H, Hyde JS. Characterization of continuously distributed cortical water diffusion rates with a stretched-exponential model. Magn. Reson. Med 2003; 50(4): 727–734. [PubMed: 14523958]
99. Ozarslan E, Basser PJ, Shepherd TM, Thelwall PE, Vemuri BC, Black- band SJ. Observation of anomalous diffusion in excised tissue by characterizing the diffusion-time dependence of the MR signal. J. Magn. Reson 2006; 183(2): 315–323. [PubMed: 16962801]
100. Hall MG, Barrick TR. From diffusion-weighted MRI to anomalous diffusion imaging. Magn. Reson. Med 2008; 59(3): 447–455. [PubMed: 18224695]
101. Kiselev VG, Il'yasov KA. Is the 'biexponential diffusion' biexponential? Magn. Reson. Med 2007; 57(3): 464–469. [PubMed: 17326171]

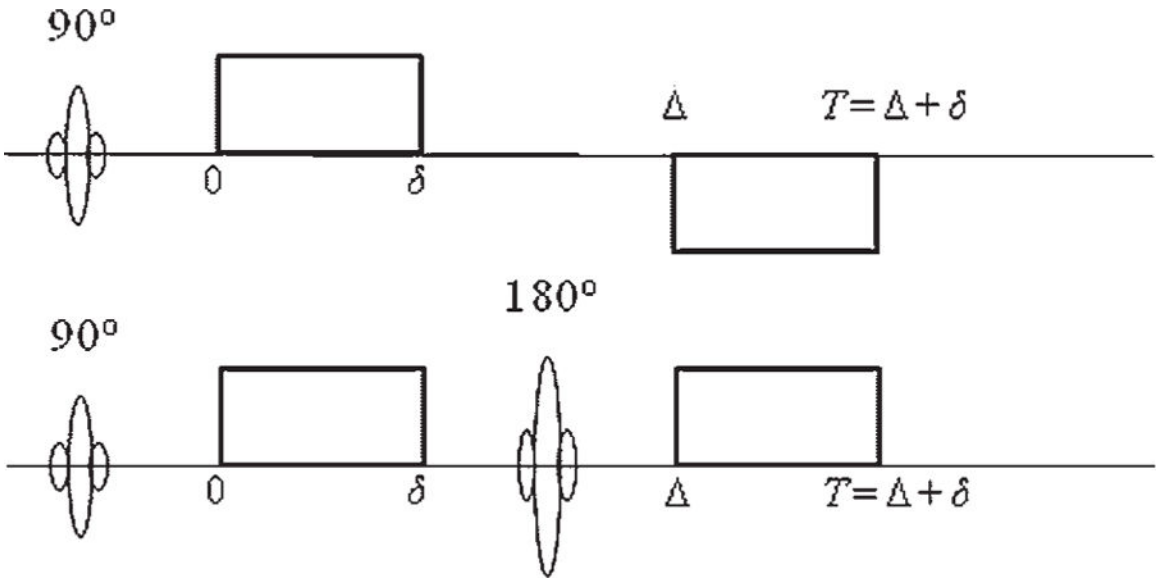

Figure 1.

Two versions of Stejskal-Tanner pulse sequence employed to sensitize the MR signal to molecular diffusion. Characteristic parameters of the waveform are the gradient amplitude G, the diffusion time Δ and the pulse width δ. The encoding (first) and decoding (second) gradient pulses have either opposite polarity (upper diagram) or are separated by a 180° refocusing RF pulse (lower diagram).

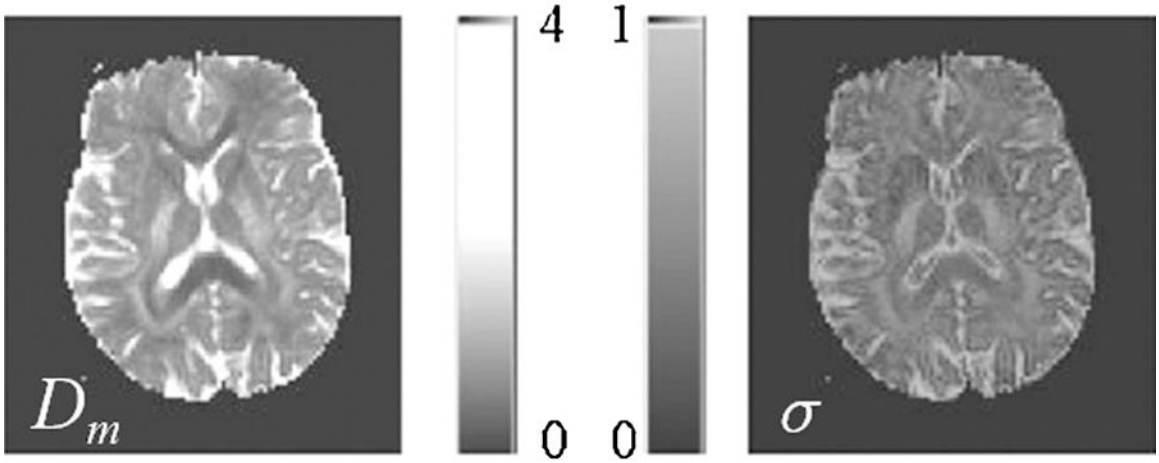

Figure 2.

An example of diffusion data obtained from the human brain using the statistical model, Eq. [28]. Images represent maps of the Gaussian peak maximum, D_m, and width, σ, corresponding to a diffusion sensitizing gradient direction perpendicular to the imaging slice orientation. The scale bars provide references for D_m (from 0 to 4 $\mu m^2/ms$) and σ (from 0 to 1 $\mu m^2/ms$). [Modified from (15)].

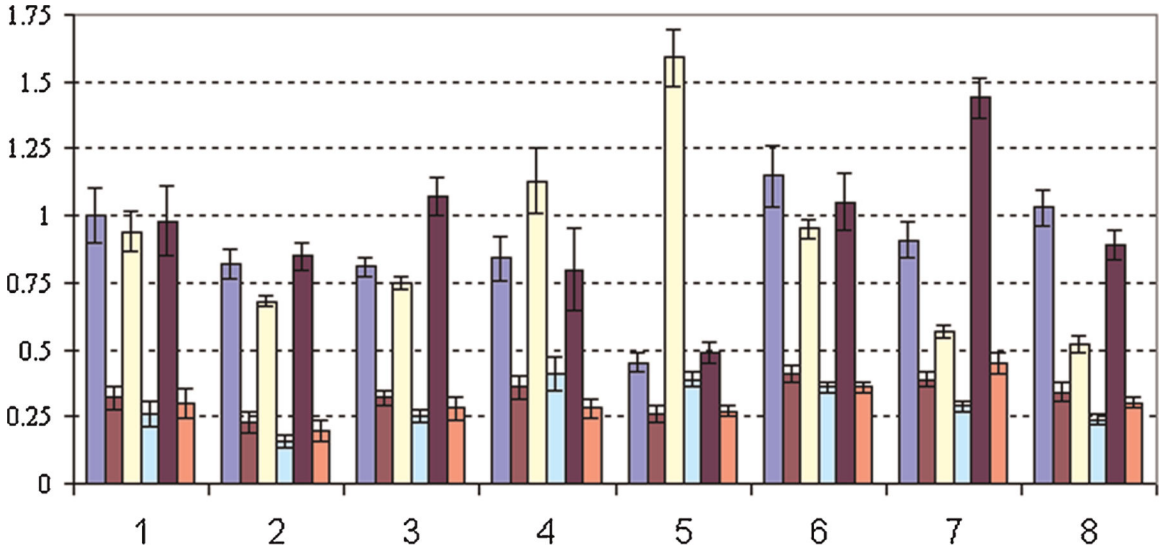

Figure 3.

Examples of diffusion data obtained from the human brain using the statistical model, Eq. [28]. Columns represent D_m and σ pairs in three different directions. The units shown are $\mu m^2/ms$. Results are grouped in eight blocks each representing an ROI: 1--frontal GM, 2--head of caudate nucleus, 3--thalamus, 4--occipital-temporal GM, 5--splenium of corpus callosum, 6--occipital WM, 7--frontal WM, 8--external capsule. In each block the first and second columns represent D_m and σ corresponding to diffusion perpendicular to slice; the third and fourth – in read-out direction (horizontal in Fig. 2); the fifth and sixth columns – in phase-encoding direction (vertical in Figure 2). Error bars represent variability across the ROI, usually about 10 voxels in size. [Reproduced from (15)].

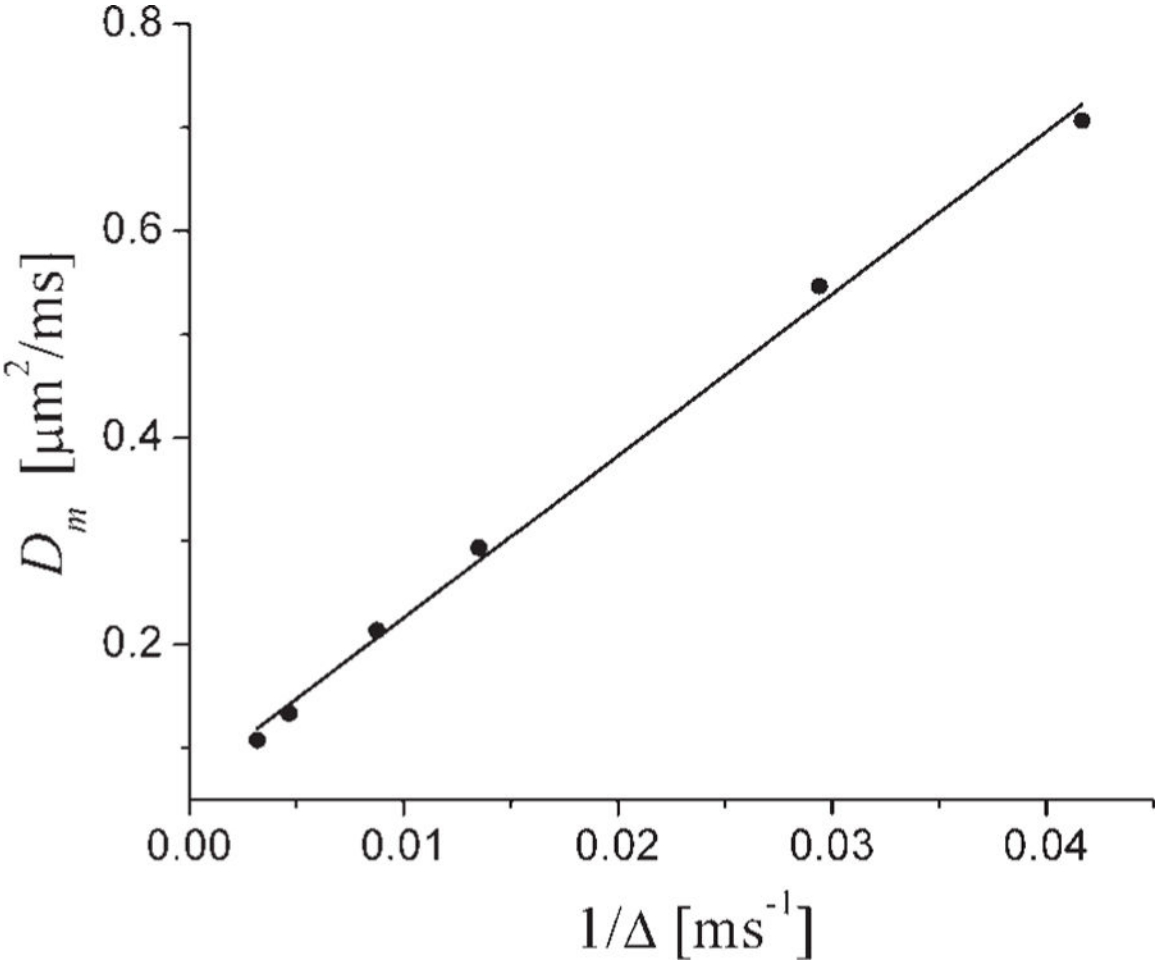

Figure 4.

Position of D_m, the maximum of the distribution function $P(D)$, found from the experimental data on HeLa cells, as a function of the inverse diffusion time Δ (symbols); solid line--linear regression. (Courtesy of Lin Zhao).

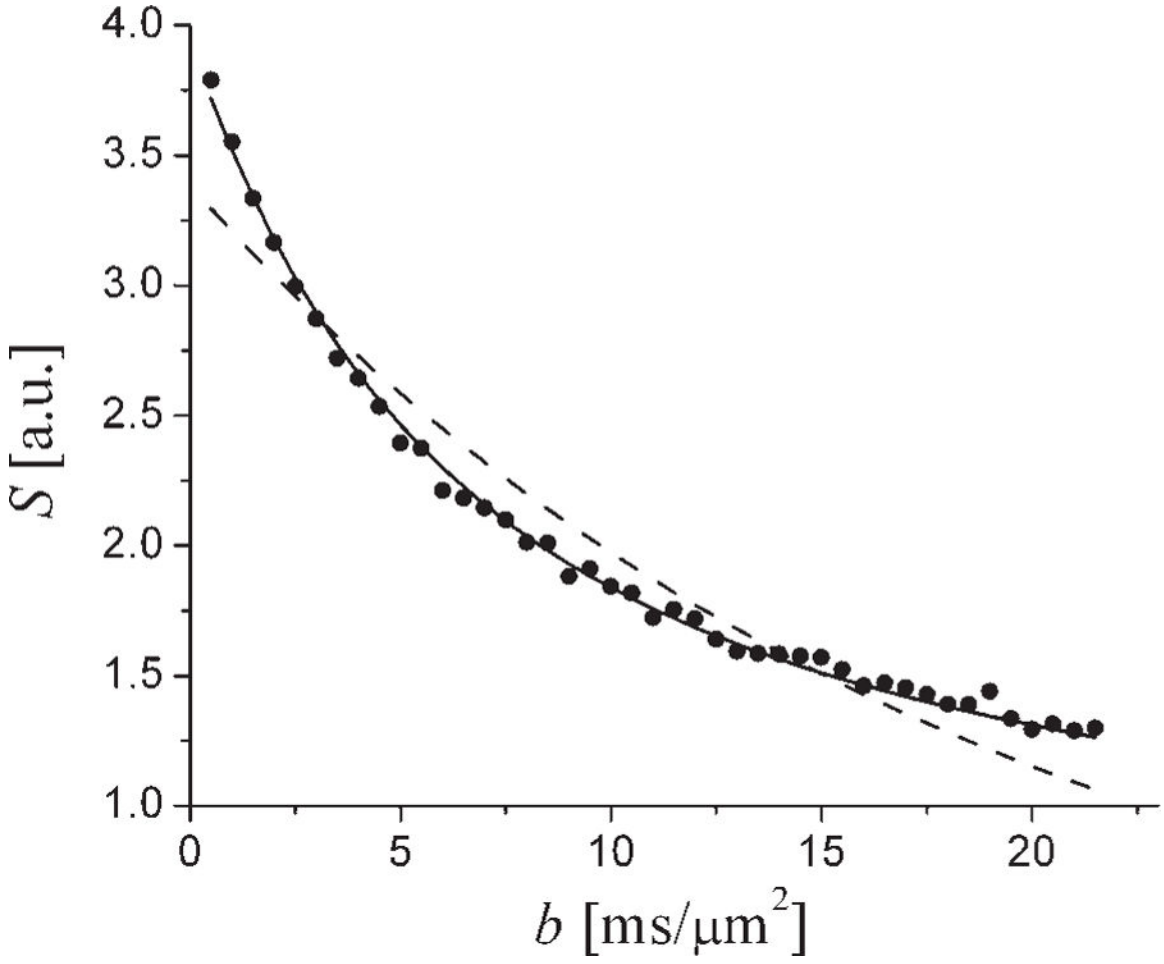

Figure 5.

Fit of the model function, Eq. [40], (solid line) to the NAA MR signal obtained from a large voxel in a rat brain. The best fit mono-exponential is displayed as a dashed line. It is essential that Eq. [40] has only two fitting parameters--S_0 and D_L, yet can provide a practically ideal fit to the data over a rather large range of b-values. [Modified from (16)].

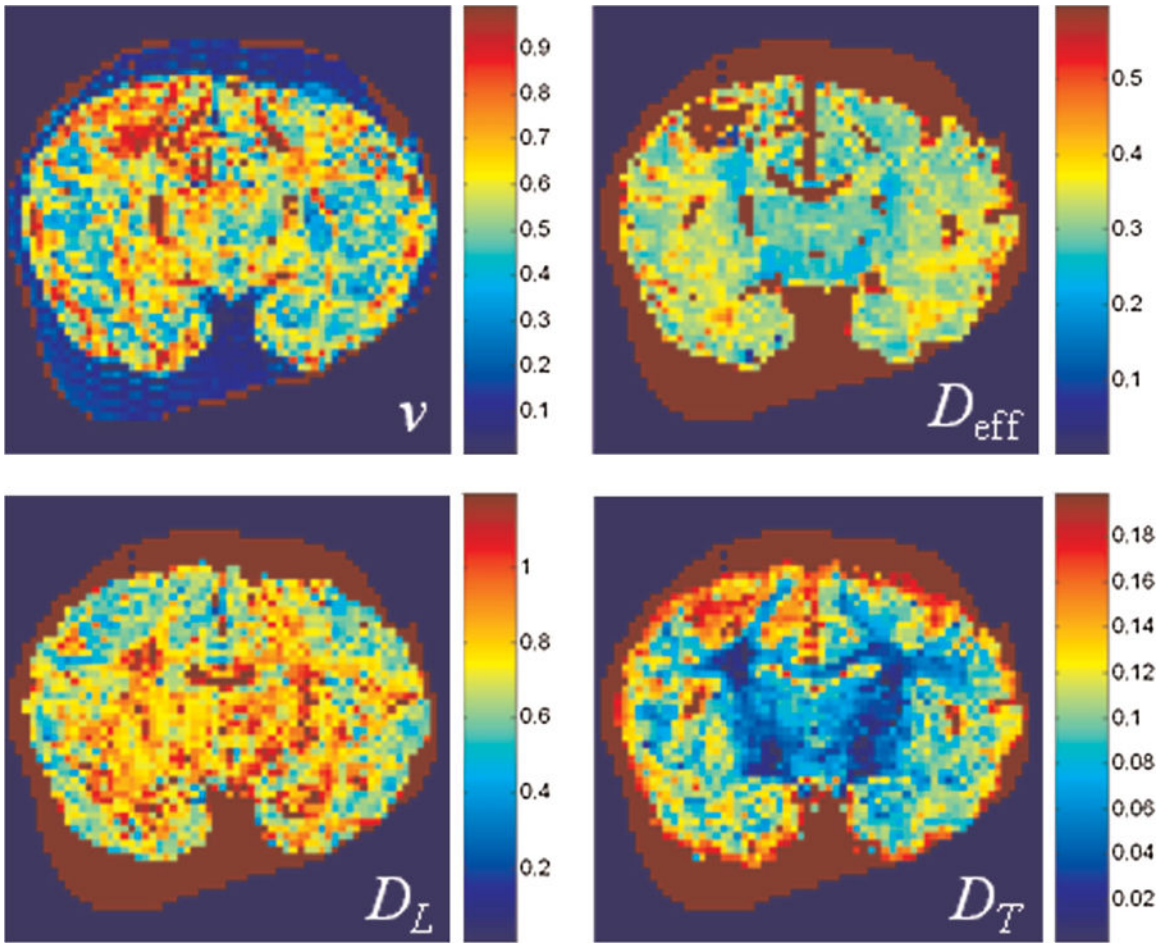

Figure 6.

Maps of the estimated model parameters obtained from a newborn primate brain: v- the volume fraction of cylindrical cells (dendrites and axons); D_{eff} --effective diffusion coefficient in the extra-cylindrical space; D_L, and D_T- longitudinal and transverse diffusion coefficients of water in the cylindrical cells. All diffusion coefficients in $\mu m^2/ms$. [Reproduced from (18)].

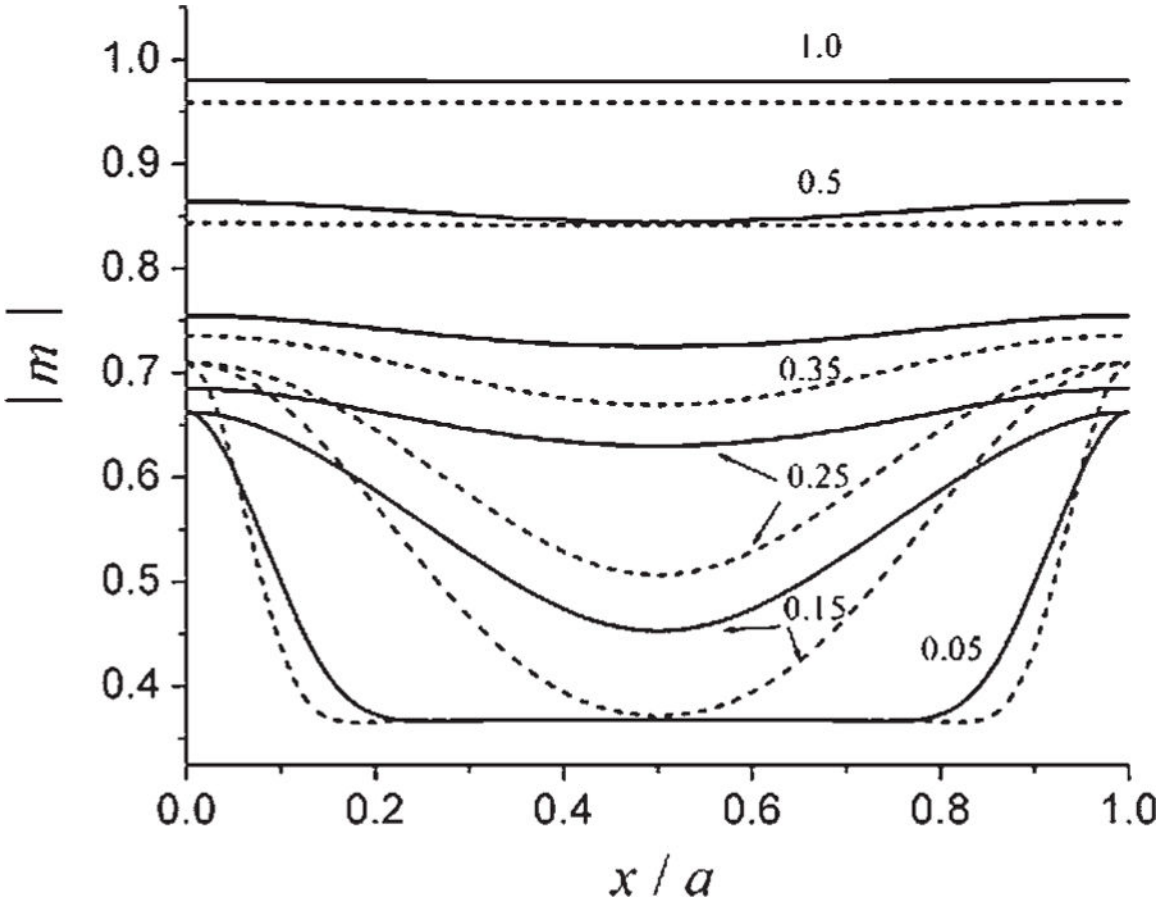

Figure 7.

The amplitudes of the local magnetization $|m|$ in a single compartment model as functions of the reduced coordinate x/a for the SE (solid lines) and NP (dashed lines) signals for different values of the parameter $\alpha = (\Delta/t_D)^{1/2}$ (identified by numbers near the corresponding curves); b-value is fixed at $bD_0 = 1$. [Modified from (84)].

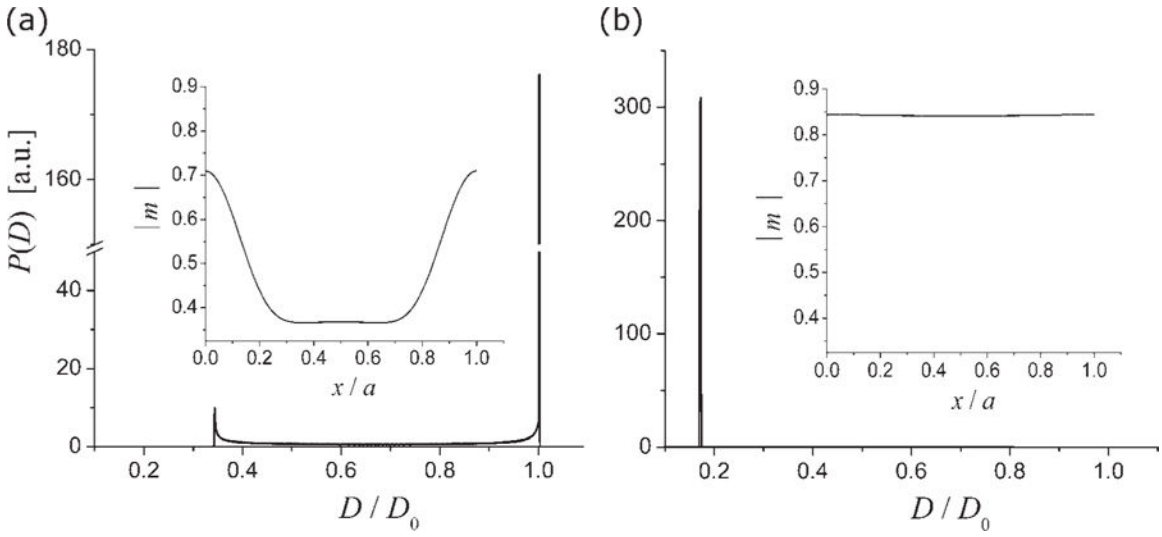

Figure 8.

The distribution functions $P(D)$ of 'local ADCs' for NP signal in a single compartment model. (a) For short diffusion times, $\Delta = 0{:}01\ t_D$, the two peaks correspond to slow and fast diffusing pools originating from an inhomogeneous distribution of magnetization; (b) for $\Delta = t_D$ the distribution of magnetization is homogeneous resulting in a single peak with a low diffusion coefficient. Insets represent corresponding distributions of magnetization $|m|$ as functions of the reduced coordinate x/a.

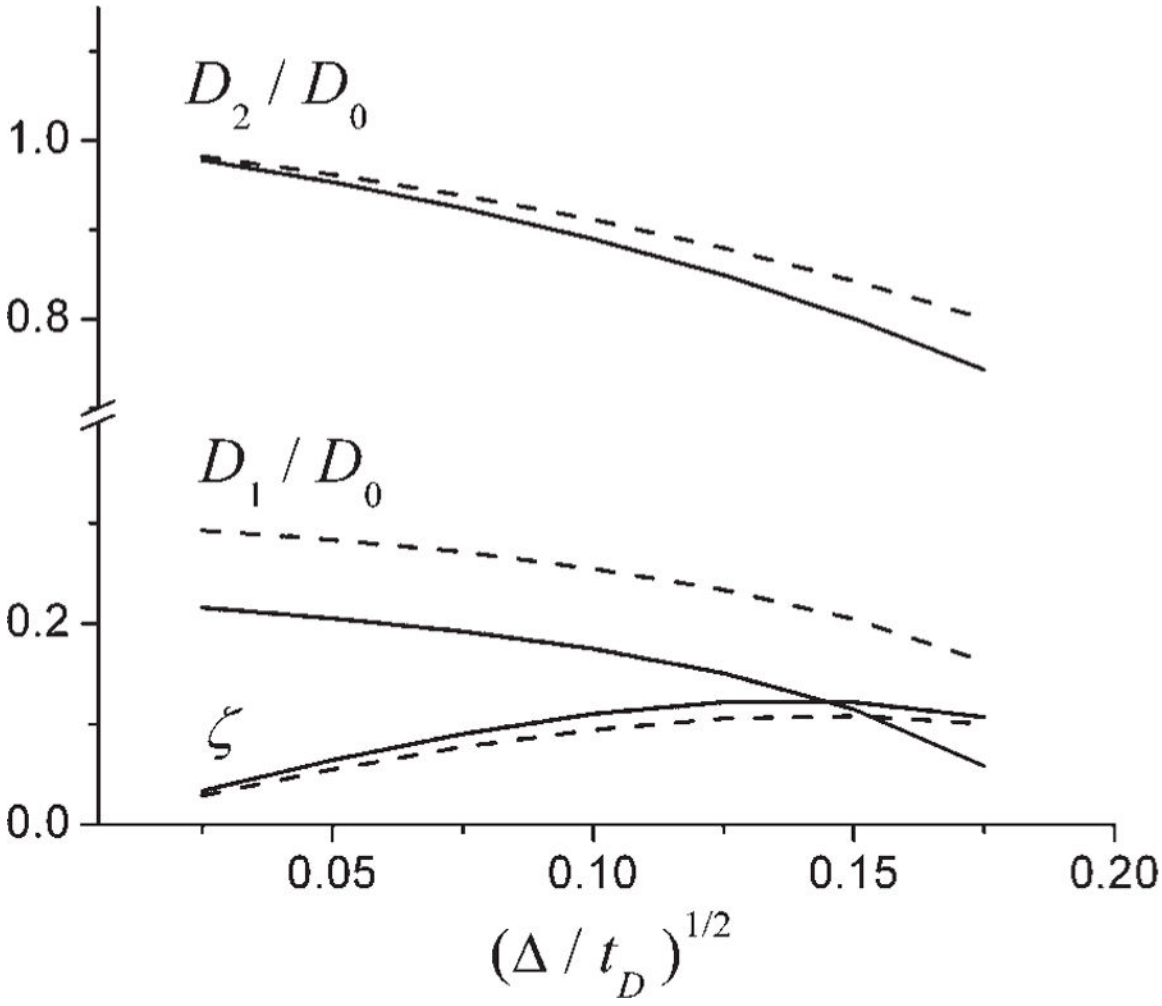

Figure 9.

Single compartment model. Diffusion time dependence of the diffusion coefficients D_1 and D_2, corresponding to the slow- and fast-diffusing pools, and the volume fraction of the slow-diffusion pool z. Solid and dashed lines correspond to $\delta = \Delta$ (SE signal) and $\delta << \Delta$ (NP signal), respectively.

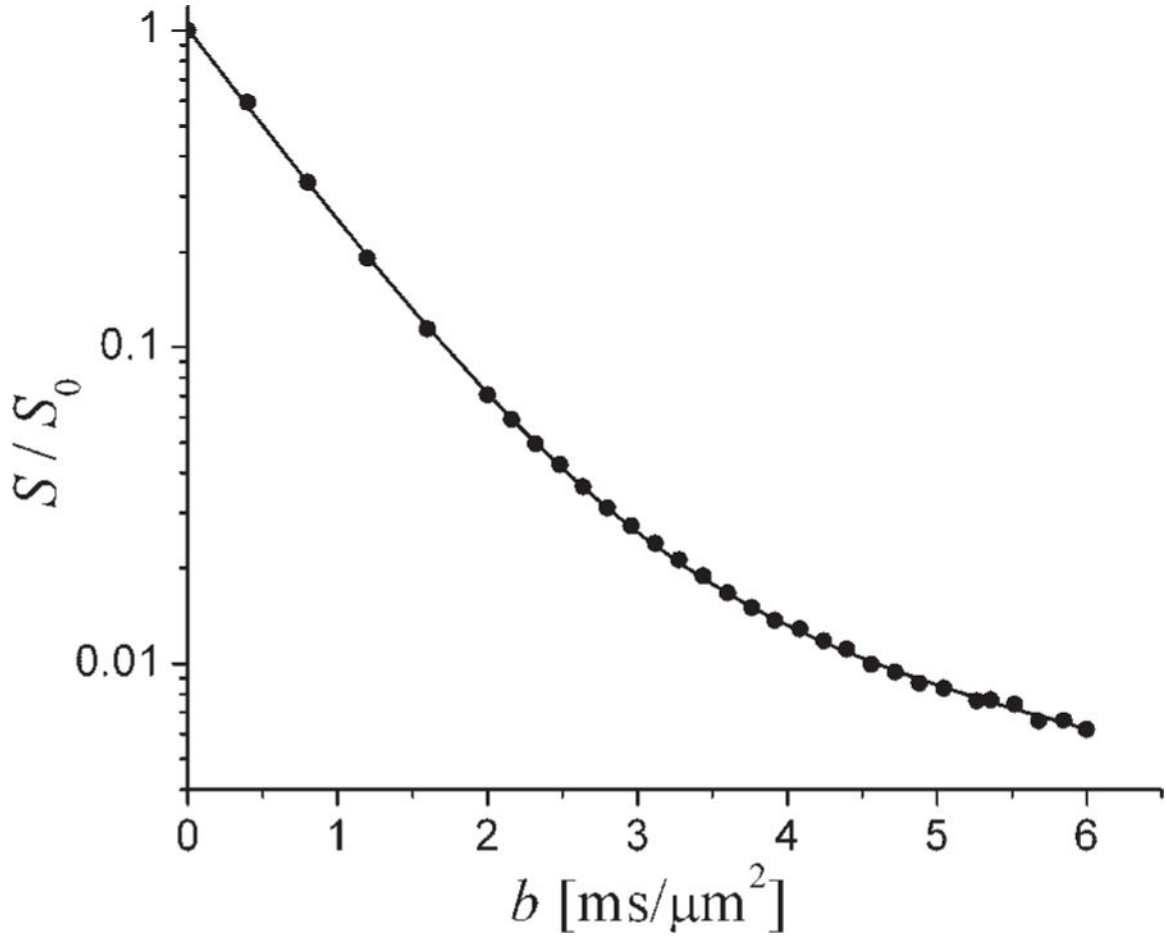

Figure 10.

The fit of a bi-exponential function to the signal obtained experimentally from water in a cylindrical tube of radius 160 μm at short diffusion time, $\alpha = (\Delta/t_D)^{1/2} = 0.1$. The fitting parameters are: $\zeta = 0.014, D_1/D_0 = 0.067, D_2/D_0 = 0.80$. (Courtesy of M. Milne and M. Conradi).

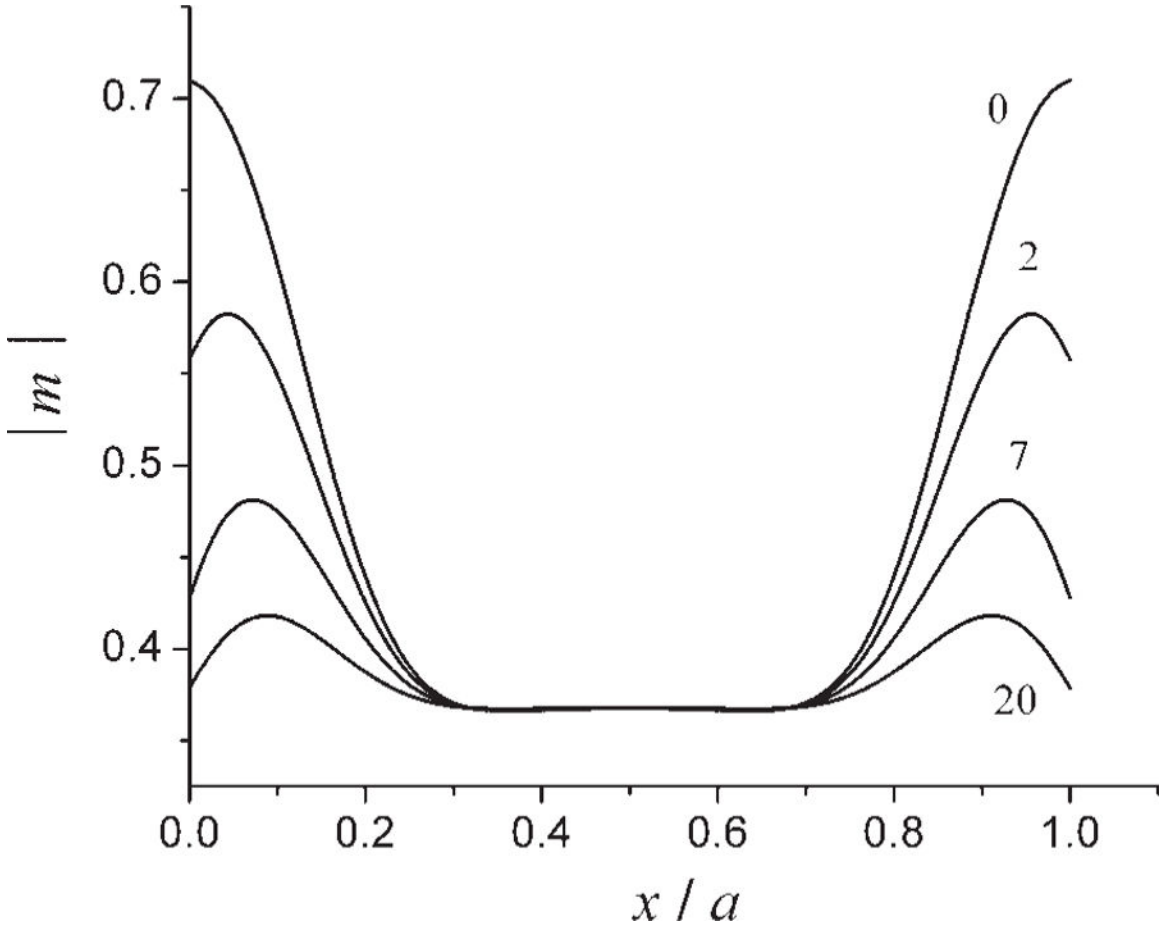

Figure 11.

1D model with permeable boundaries. The magnetization distribution at short diffusion times for different values of reduced permeability $\mu a/D_0$ (identified by numbers near the corresponding curves); $\Delta/t_D = 0.01$, $bD_0 = 1$. Only one segment of the periodic structure is shown. The distribution of magnetization is non-homogeneous, as in the impermeable case (Figure 8), leading to the presence of slow and fast pools. The amplitude of the magnetization corresponding to the slow pool decreases with increased permeability due to the increase of diffusivity caused by spin exchange across the boundaries.

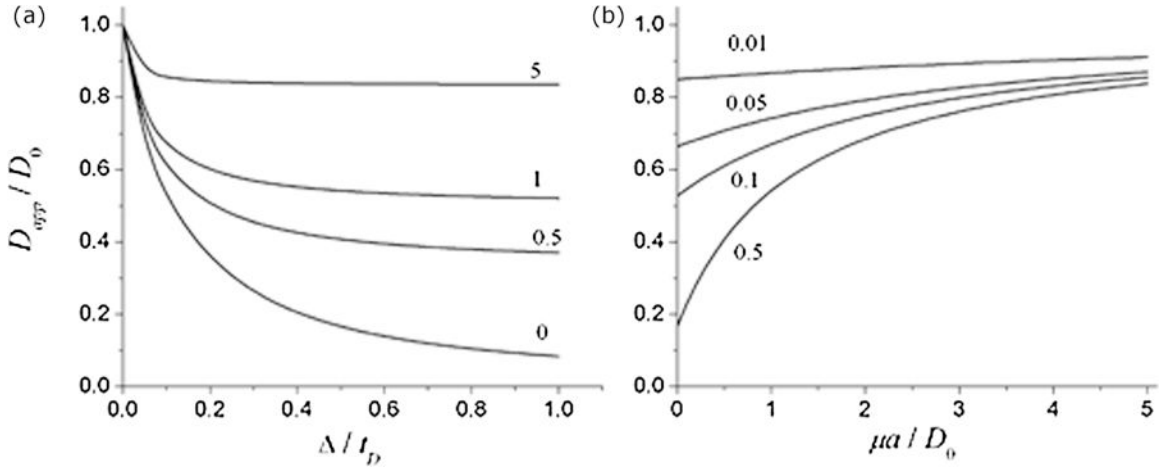

Figure 12.

1D model with permeable boundaries. The dependence of ADC (a) on diffusion time Δ for different values of reduced permeability $\mu a/D_0$ (identified by numbers near the corresponding curves) and (b) on reduced permeability for different Δ/t_D (identified by numbers near the corresponding curves).

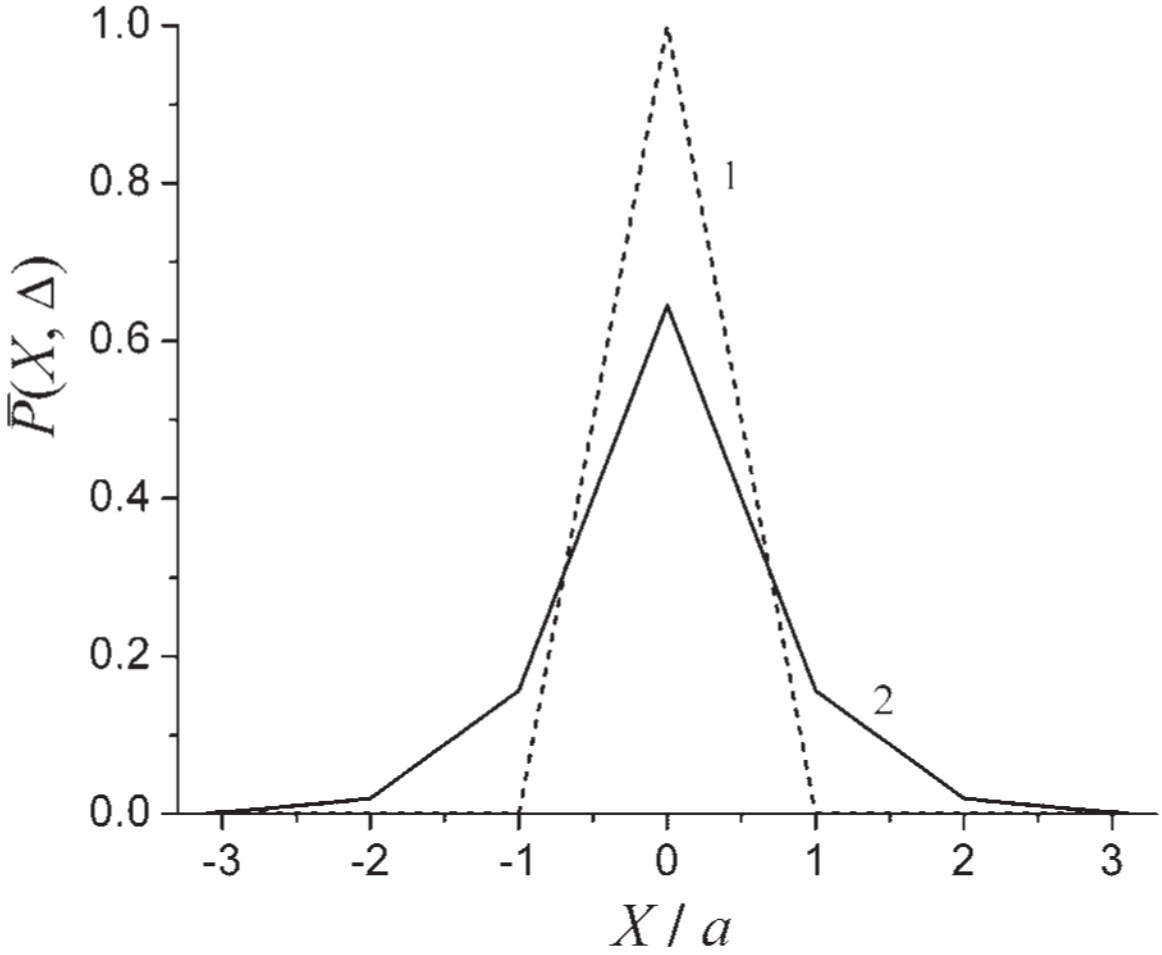

Figure 13.

q-space analysis. The average propagator $\bar{P}(X, \Delta)$ in the periodic structure for $\mu = 0$ (line 1, dashed), and $\mu\Delta/a = 0{:}25$ (line 2, solid). The shape of the solid line is suggestive of a multi-compartment system with different compartment sizes, though it actually reflects the permeable nature of boundaries in a multi-compartment system with a single compartment size. (Modified from (26)].

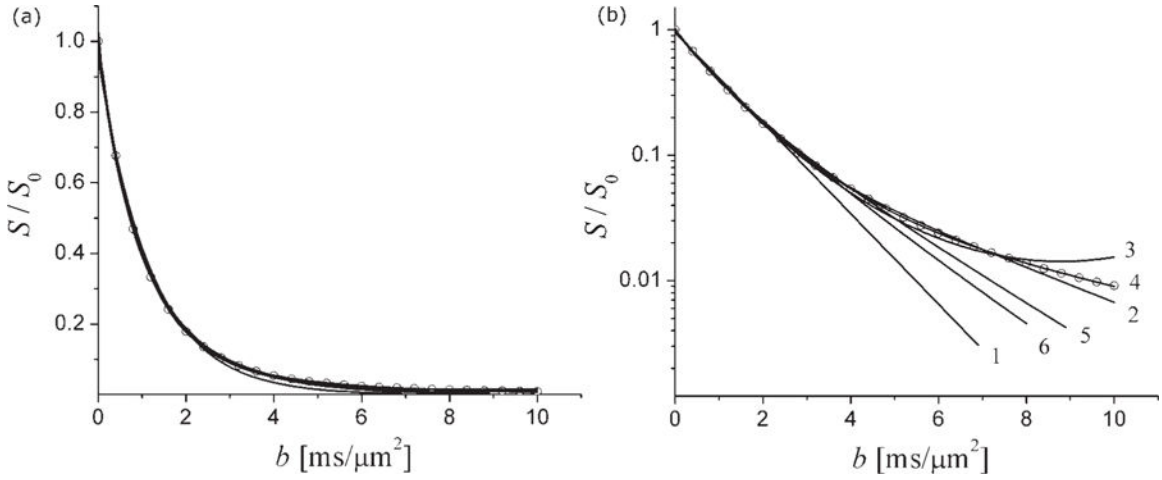

Figure 14.

Fit of different models to a signal generated by the statistical model, Eq. [28] (symbols) with $D_m = 1\ \mu m^2/ms$ and $\sigma = 0{:}4\ \mu m^2/ms$. (a)--normal scale; (b)--log scale. (1) mono-exponential model, (2) bi-exponential model, (3) cumulant expansion truncated at the first three terms (kurtosis model), (4) cumulant expansion truncated at four first terms, (5) 'cylindrical' model, Eq. [39], (6) 'stretched-exponent' model.